



# Hubble Space Telescope Images of SN 1987A: Evolution of the Ejecta and the Equatorial Ring from 2009 to 2022

Sophie Rosu<sup>1</sup> , Josefin Larsson<sup>1</sup> , Claes Fransson<sup>2</sup> , Peter Challis<sup>3</sup>, Tuomas Kangas<sup>4,5</sup> , Robert P. Kirshner<sup>6</sup> , Stephen S. Lawrence<sup>7</sup> , Peter Lundqvist<sup>2</sup> , Mikako Matsuura<sup>8</sup> , Jesper Sollerman<sup>2</sup> , George Sonneborn<sup>9</sup> , and

Linda Tenhu<sup>1</sup>

<sup>1</sup> Department of Physics, KTH Royal Institute of Technology, The Oskar Klein Centre, AlbaNova, SE-106 91 Stockholm, Sweden

<sup>2</sup> Department of Astronomy, Stockholm University, The Oskar Klein Centre, AlbaNova, SE-106 91 Stockholm, Sweden

<sup>3</sup> Center for Astrophysics | Harvard & Smithsonian, 60 Garden Street, MS-19, Cambridge, MA 02138, USA

<sup>4</sup> Finnish Centre for Astronomy with ESO (FINCA), FI-20014, University of Turku, Finland

<sup>5</sup> Tuorla Observatory, Department of Physics and Astronomy, FI-20014, University of Turku, Finland

<sup>6</sup> Thirty Meter Telescope International Observatory, 100 West Walnut Street, Pasadena, CA 91124, USA

<sup>7</sup> Department of Physics and Astronomy, Hofstra University, Hempstead, NY 11549, USA

<sup>8</sup> Cardiff Hub for Astrophysics Research and Technology (CHART), School of Physics and Astronomy, Cardiff University, Queen's Buildings, The Parade, Cardiff CF24 3AA, UK

<sup>9</sup> Observational Cosmology Laboratory, Code 665, NASA Goddard Space Flight Center, Greenbelt, MD 20771, USA

Received 2024 January 4; revised 2024 March 20; accepted 2024 March 20; published 2024 May 10

## Abstract

Supernova (SN) 1987A offers a unique opportunity to study how a spatially resolved SN evolves into a young SN remnant. We present and analyze Hubble Space Telescope (HST) imaging observations of SN 1987A obtained in 2022 and compare them with HST observations from 2009 to 2021. These observations allow us to follow the evolution of the equatorial ring (ER), the rapidly expanding ejecta, and emission from the center over a wide range in wavelength from 2000 to 11,000 Å. The ER has continued to fade since it reached its maximum  $\sim 8200$  days after the explosion. In contrast, the ejecta brightened until day  $\sim 11,000$  before their emission levelled off; the west side brightened more than the east side, which we attribute to the stronger X-ray emission by the ER on that side. The asymmetric ejecta expand homogeneously in all filters, which are dominated by various emission lines from hydrogen, calcium, and iron. From this overall similarity, we infer the ejecta are chemically well mixed on large scales. The exception is the diffuse morphology observed in the UV filters dominated by emission from the Mg II resonance lines that get scattered before escaping. The 2022 observations do not show any sign of the compact object that was inferred from highly ionized emission near the remnant's center observed with JWST. We determine an upper limit on the flux from a compact central source in the [O III] HST image. The nondetection of this line indicates that the S and Ar lines observed with JWST originate from the O free inner Si–S–Ar-rich zone and/or that the observed [O III] flux is strongly affected by dust scattering.

*Unified Astronomy Thesaurus concepts:* Core-collapse supernovae (304); Supernova remnants (1667); Circumstellar matter (241); Shocks (2086); Ejecta (453)

## 1. Introduction

Supernova (SN) 1987A in the Large Magellanic Cloud (LMC), discovered on 1987 February 23, is the closest naked-eye SN since Kepler's SN in 1604 (see Arnett et al. 1989; McCray 1993; McCray & Fransson 2016, for reviews). This unique event became one of the most deeply studied astronomical objects in the Universe outside of our solar system, from ground to space, at all wavelengths. Its evolution from SN to supernova remnant (SNR) has notably been followed by the Hubble Space Telescope (HST) since its launch in 1990 with an excellent spatial resolution (see, e.g., Larsson et al. 2019a, and references therein).

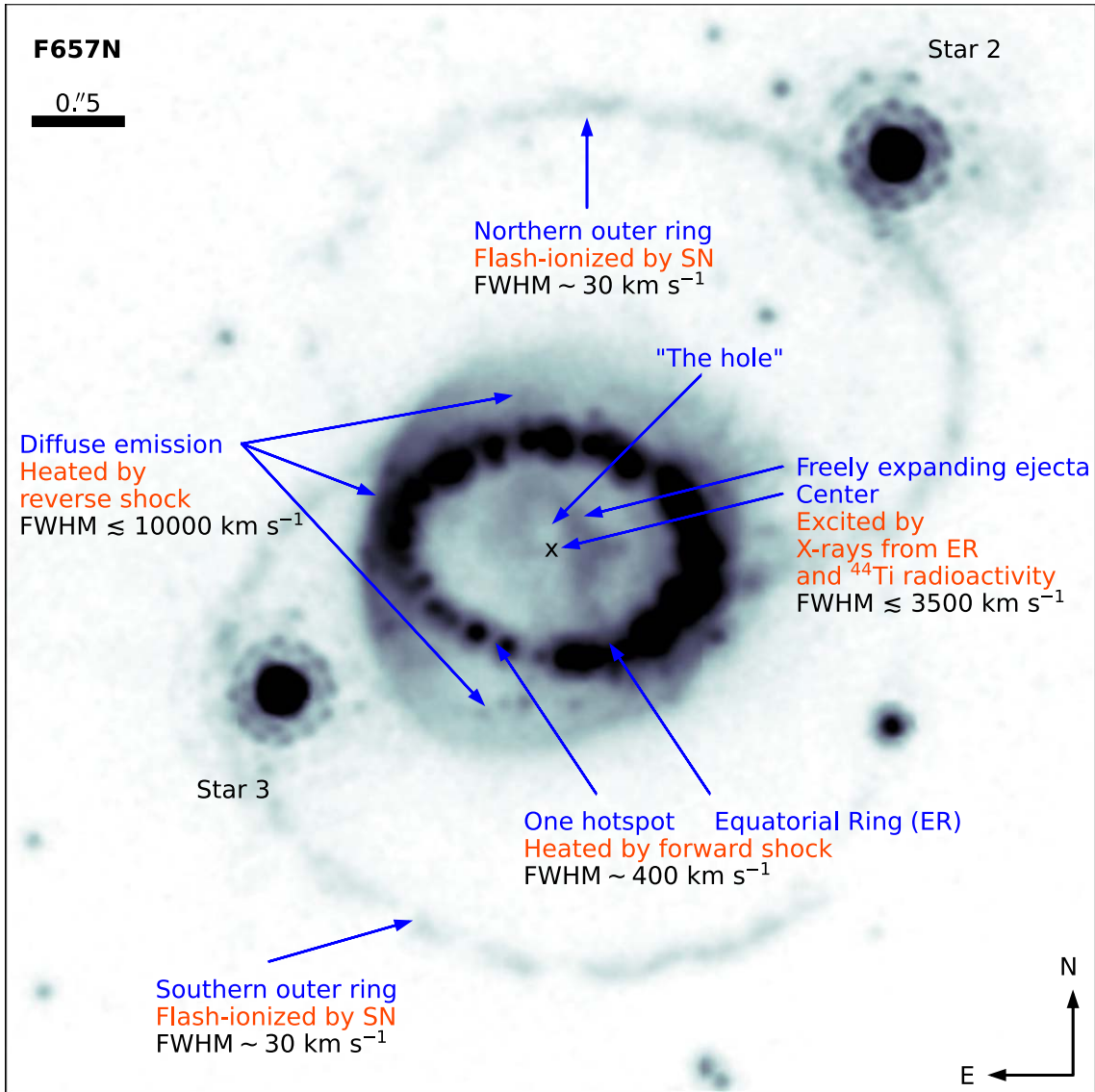
The resolved view offered by the HST images taken with the Wide Field Camera 3 (WFC3) shows the ejecta expanding into the circumstellar triple-ring nebula (see Figure 1). The inner equatorial ring (ER) has a radius of  $\sim 0''.8$ , while the fainter outer rings have radii almost 3 times larger and are offset from the equatorial plane (Tziamtzis et al. 2011, their Figure 5). The three

rings are inclined by an angle ranging between  $38^\circ$  and  $45^\circ$  (Tziamtzis et al. 2011),  $43^\circ$  being the most probable value for the ER inclination, with the northern part being the near side (Panagia et al. 1991; Plait et al. 1995; Sugerman et al. 2005). The preshock expansion velocities of the rings imply they were ejected  $\sim 20,000$  yr before the explosion (Crofts & Heathcote 2000). The formation of the triple ring was likely connected to a binary merger (Morris & Podsiadlowski 2007, 2009).

Figure 1 illustrates the asymmetric, dense inner ejecta, which are expanding freely inside the ER, as well as the shock interaction between the fast outer ejecta and the circumstellar medium (CSM). The key properties of the different emission components are summarized in Figure 1. The velocity of the freely expanding ejecta ( $v_{ej}$ ) is given by

$$v_{ej} = 858 \left( \frac{t}{10,000 \text{ days}} \right)^{-1} \left( \frac{d}{0''.1} \right) \text{ km s}^{-1}, \quad (1)$$

where  $t$  is the time since the explosion, and  $d$  is the angular distance from the geometric center (marked with a cross in Figure 1), assuming a distance to the LMC of 49.59 kpc (Pietrzyński et al. 2019). The most recent epoch considered in this paper is  $t \sim 13,000$  days, which implies that  $v_{ej} \sim 5300 \text{ km s}^{-1}$  at the



**Figure 1.** HST/WFC3 2022 image of SN 1987A in the F657N filter with labels showing the main emission components (dark blue) and corresponding processes responsible for these emissions (orange). The FWHM of the optical emission lines are indicated in black (from Gröningsson et al. 2008; Tziamtzis et al. 2011; Fransson et al. 2013; Larsson et al. 2019a). The image was scaled by an asinh function to highlight the weak emission outside the ER. The field of view is  $6''.0 \times 6''.0$ . The cross represents the geometric center of the ER (Alp et al. 2018).

semimajor axis of the ER ( $0''.8$ ). Ejecta with higher velocities have already interacted with the ER, giving rise to hotspots in the ER, smaller spots outside the ER, as well as diffuse emission from the reverse shock. The morphology of the reverse shock was recently reconstructed in 3D based on James Webb Space Telescope (JWST) NIRSpec data, which showed that it extends from the inner edge of the ER to higher latitudes on both sides, forming a bubble-like structure (Larsson et al. 2023). The emission from the reverse shock at high latitudes is projected outside the ER in Figure 1.

The very first hotspot in the ER appeared in 1995 in the northeast region, as a consequence of the SN blast wave crashing into the ER (Sonneborn et al. 1998; Lawrence et al. 2000). Additional spots appeared in the following years to reach a total of approximately  $28^{10}$  covering the whole ER at 12,980 days (C. Tegkelidis et al. 2024, in preparation). These

spots indicate the presence of gas clumps of higher density than the surrounding gas (Gröningsson et al. 2008). The SN ejecta, through their interaction with the ER, are now dissolving the hotspots (Fransson et al. 2015).

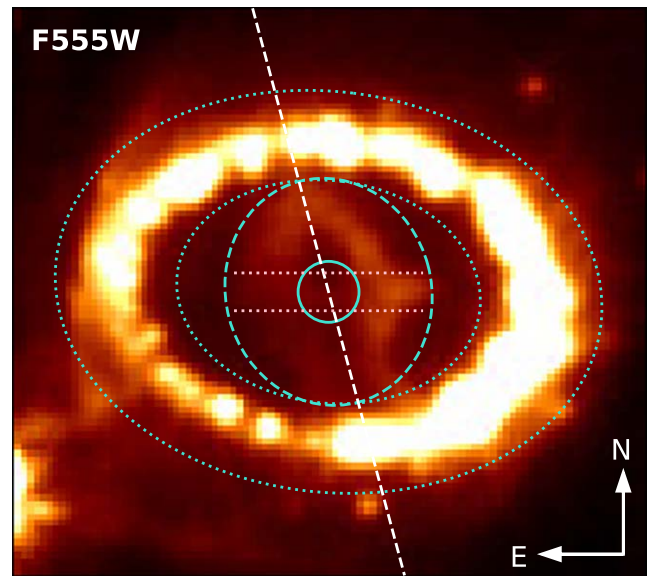
An increase in the optical fluxes in the ER was observed until about 8300 days after the explosion, followed by a decrease pretty much linear in time (Fransson et al. 2015; Larsson et al. 2019a). A similar behavior was observed at all wavelengths—apart from radio and hard X-rays, which are still increasing in flux (Cendes et al. 2018; Alp et al. 2021; Maitra et al. 2022). New small spots outside the ER show that the blast wave has propagated beyond the ring (Larsson et al. 2019a; Arendt et al. 2023). Signs of shock interaction outside the ER are also clearly seen in JWST/NIRCam images (Arendt et al. 2023). The recent JWST/NIRSpec and JWST/MRS observations show that the inner ejecta have recently started to interact with the reverse shock at the inner edge of the ER in the southwest (Fransson et al. 2024).

<sup>10</sup> Out of these bright spots in the ER, the one in the southwest nearest  $PA = 230^\circ$  is a star projected on the ER.

The regular monitoring by HST has provided a detailed record of the ejecta evolution. When the HST observations started in the early 1990s, the dominant radioactive isotope supplying energy input to the ejecta was  $^{44}\text{Ti}$ . This resulted in a slowly decreasing optical luminosity until about 5000 days after the explosion. The optical luminosity then started to increase in both the red and blue optical bands owing to the absorbed and thermalized X-rays from the ejecta interacting with the ring (Larsson et al. 2011), marking the transition to the SNR phase. This transition is also marked by the change of morphology of the ejecta from a centrally dominated emission elongated in the northeast–southwest direction to a “horseshoe-like” shape. This horseshoe is irregularly elongated in the same direction but with a brightening of the outer limb, with the northern (respectively southern) lobe being predominantly blueshifted (respectively redshifted; see Figure 1; but also Fransson et al. 2013; Larsson et al. 2013). The observed morphology of the ejecta is also expected to be affected by dust, which was observed by Herschel and Atacama Large Millimeter/submillimeter Array (Matsuura et al. 2015; Cigan et al. 2019).

A major new advancement in the study of SN 1987A is the recent JWST observations that revealed the first unambiguous electromagnetic signal due to the compact object created in the explosion (Fransson et al. 2024). The observations show narrow, ionized emission lines from [Ar II], [Ar VI], [S III], and [S IV] at the center of the system, which can only be explained by ionization of the innermost, slow-moving ejecta by a compact central source. The exact nature of this source is yet to be determined, with the most likely scenarios being either a pulsar wind nebula (PWN) or a cooling neutron star (CNS). Emission lines associated with the compact object are expected also at optical wavelengths, and it is therefore of great interest to search for signs of this emission in the recent HST observations (see Alp et al. 2018, for previous upper limits). The probability of detecting the central source increases with time due to the expansion of the ejecta, which leads to gradually decreasing background emission as well as decreasing optical depth of the dust. We note that the central source may be revealed as a general diffuse brightening in the central region rather than as a point source if the effects of dust scattering are important.

As part of a long-term monitoring program, SN 1987A was observed in 2022 September (days 12,978–12,980 after the explosion) by HST/WFC3 in nine filters, which cover the entire wavelength region between 2000 and 11,000 Å. It is the first time that HST imaging observations of SN 1987A cover the full optical domain since 2009 (8329 days after the explosion). We make use of these and earlier archival observations to study the recent evolution of the broadband and narrowband photometry and morphology of the ejecta between days 8329 and 12,980. We also use the annual imaging in the F438W and F625W filters to provide light curves of the system, which adds 4 yr of data compared to that from Larsson et al. (2019a). These different measurements reveal the asymmetric explosion geometry in increasingly great detail and provide information on the evolving energy sources. The latter are predicted to affect the temporal evolution in different ways. The energy input from the decay of  $^{44}\text{Ti}$  will lead to a gradual fading across the whole ejecta. Any significant contribution from the compact object would manifest as a brightening of the central region and a change of the relative



**Figure 2.** HST/WFC3 2022 image of SN 1987A in the F555W filter together with the regions adopted to compute the fluxes. The dotted cyan lines define the elliptical annulus around the ER, while the dashed and solid cyan lines define the elliptical region around the ejecta and the circular region around the center, respectively (see Section 5). The regions for the ejecta and the center were expanded over time to account for the expansion of the ejecta. The white dashed line represents the separation between eastern and western parts. The pink dotted lines represent the horizontal region adopted for Figure 13. The image was scaled by an asinh function to highlight the weak emission outside the ER. The field of view is  $2''.50 \times 2''.25$ .

brightness of different photometric bands. Finally, the energy input from X-rays from the ER is expected to give rise to changes in flux and morphology that reflect the X-ray evolution of the ER, as well as a general limb-brightened morphology (according to the model in Fransson et al. 2013).

This paper is organized as follows. We describe the new 2022 HST observations and the data reduction process in Section 2. We discuss the lines contributing to the different filters in Section 3. The change of morphology of SN 1987A from days 8329 to 12,980 is presented in Section 4, while broadband and narrowband photometry in three different regions, namely the ER, ejecta, and center (see the apertures delineated in Figure 2) is presented in Section 5. Section 6 is devoted to the analysis of the light curve of SN 1987A from day 8329 to 12,980 in the same three regions in the F438W and F625W filters. The results are discussed in Section 7, and we provide our conclusions in Section 8. Throughout this paper, the distance to SN 1987A is taken to be 49.59 kpc (Pietrzyński et al. 2019), and we refer to spectral lines by their vacuum wavelengths.

## 2. Observations and Data Reduction

The HST/WFC3 observations analyzed in this paper consist of nine new images taken in 2022 September, eight archival images taken in 2009 December (seven out of these used filters in common with the 2022 images), and 20 archival images taken every year between 2011 and 2021, except in 2012, in the two broadband filters F438W and F625W (details provided in Table 1). In Table 2, we provide the passband rectangular widths and the pivot wavelengths of the ten different filters. The HST observations between days 8329 and 11,458 were analyzed in a series of papers to which we refer for more detailed information (Larsson et al. 2011; Larsson et al. 2013;

**Table 1**  
Details of the HST/WFC3 Observations

Date (YYYY MMM DD)	Epoch (days)	Filter	Exposure Time (s)
2009 Dec 13	8329	F225W	800
2009 Dec 13	8329	F336W	800
2009 Dec 13	8329	F438W	800
2009 Dec 12	8328	F502N	6200
2009 Dec 13	8329	F555W	400
2009 Dec 12	8328	F625W	3000
2009 Dec 13	8329	F657N	1600
2009 Dec 13	8329	F814W	400
<hr/>			
2011 Jan 05	8717	F438W	1400
2011 Jan 05	8717	F625W	1140
2013 Feb 06	9480	F438W	1200
2013 Feb 06	9480	F625W	1200
2014 Jun 15	9974	F438W	1200
2014 Jun 15	9974	F625W	1200
2015 May 24	10,317	F438W	1200
2015 May 24	10,317	F625W	1200
2016 Jun 08	10,698	F438W	600
2016 Jun 08	10,698	F625W	600
2017 Aug 03	11,119	F438W	1400
2017 Aug 03	11,119	F625W	1200
2018 Jul 08	11,458	F438W	1200
2018 Jul 08	11,458	F625W	1200
2019 Jul 22	11,837	F438W	1200
2019 Jul 22	11,837	F625W	1200
2020 Aug 06	12,218	F438W	1160
2020 Aug 06	12,218	F625W	1160
2021 Aug 21	12,598	F438W	1200
2021 Aug 21	12,598	F625W	1080
<hr/>			
2022 Sep 06	12,979	F275W	2800
2022 Sep 06	12,979	F280N	5600
2022 Sep 06	12,979	F336W	2600
2022 Sep 05	12,978	F438W	1200
2022 Sep 07	12,980	F502N	5600
2022 Sep 05	12,978	F555W	1080
2022 Sep 05	12,978	F625W	1080
2022 Sep 06	12,979	F657N	2600
2022 Sep 05	12,978	F814W	1080

**Note.** Columns (1) and (2) give the date of observation and the epoch measured in number of days since the explosion on 1987 February 23. Columns (3) and (4) give the filter and exposure time of the observation. The new WFC3 images are presented in the bottom section.

France et al. 2015; Fransson et al. 2015; Alp et al. 2018; Larsson et al. 2019a).

The dithered exposures were combined using *DrizzlePac* (Ferland et al. 2013) adopting a pixel scale of  $0''.025$ . Cosmic rays were removed, and distortion corrections were applied as part of the drizzling process (Gonzaga et al. 2012). The HST astrometry was corrected by aligning field stars with GAIA as in Larsson et al. (2019a). The images were aligned to the same pixel frame using *astropy reproject* with bilinear interpolation.

### 3. Line Contributions to the Different Filters

To identify which lines contribute to the different filters, we present in Figure 3, together with the filters' response functions, the Space Telescope Imaging Spectrograph (STIS) spectra from 2017 of the ER and the ejecta discussed in Kangas

**Table 2**  
Properties of the HST/WFC3 Filters

Filter	Width <sup>a</sup> (Å)	Pivot Wavelength <sup>b</sup> (Å)
F225W	467	2372
F275W	405	2710
F280N	42	2833
F336W	512	3355
F438W	615	4326
F502N	65	5010
F555W	1565	5308
F625W	1465	6243
F657N	121	6567
F814W	1565	8039

**Notes.** Columns (1), (2), and (3) give the name, the passband rectangular width, and the pivot wavelength of the filter, respectively.

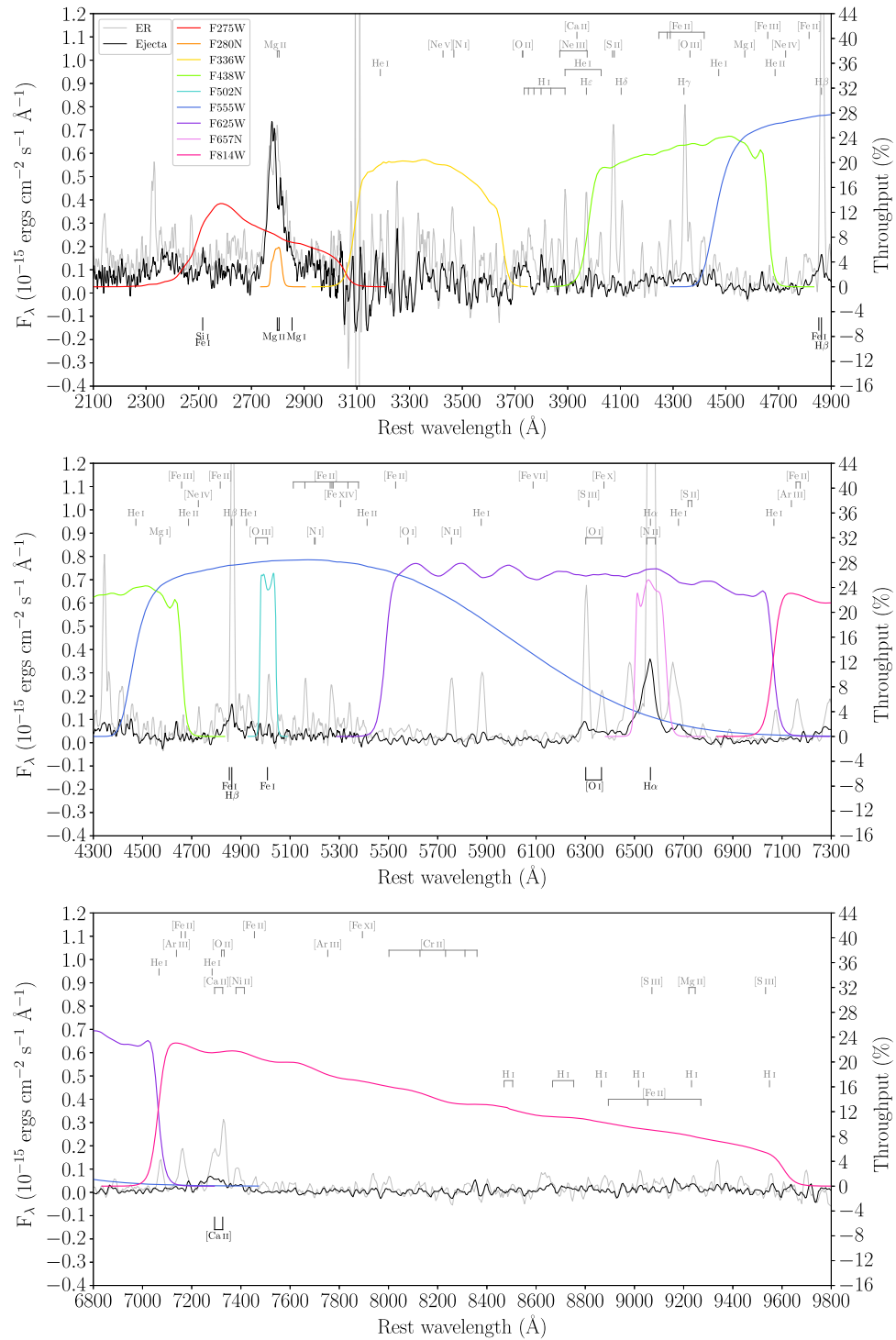
<sup>a</sup> Defined as the equivalent width divided by the maximum throughput within the filter bandpass.

<sup>b</sup> Measure of the effective wavelength of a filter, calculated based on the integrated system throughput.

et al. (2022). The STIS spectra were obtained from two adjacent  $0''.2$  wide slits oriented in the north–south direction. The extraction regions cover most of the inner ejecta, as well as the north and south parts of the ER. We added the fluxes in the two slits to form the spectra shown in Figure 3. We used the STIS spectra here despite their relatively low signal-to-noise ratio (S/N) because they are the most recent spectra covering the whole wavelength region considered here. Higher S/N optical spectra of the ejecta taken at earlier times (1995) were modeled in Jerkstrand et al. (2011). We refer to this paper for the identification of lines that are close to noise level in the 2017 spectra. The optical spectra of the ER and the ejecta are both dominated by line emission; the continuum only contributes a small amount to the total flux in any spectral region or filter (see Gröningsson et al. 2008; Jerkstrand et al. 2011).

The narrowband filters are mostly dominated by a single line: Mg II  $\lambda\lambda$  2795, 2802 in F280N, Fe I  $\lambda$  5007 (ejecta) or [O III]  $\lambda$  5008 (ER) in F502N, and H $\alpha$  in F657N. The narrow lines from the ER are fully contained by the filters (except for F280N), while the broad ejecta lines are not. The velocity ranges for the main emission lines in the F280N, F502N, and F657N filters are given in Table 3.

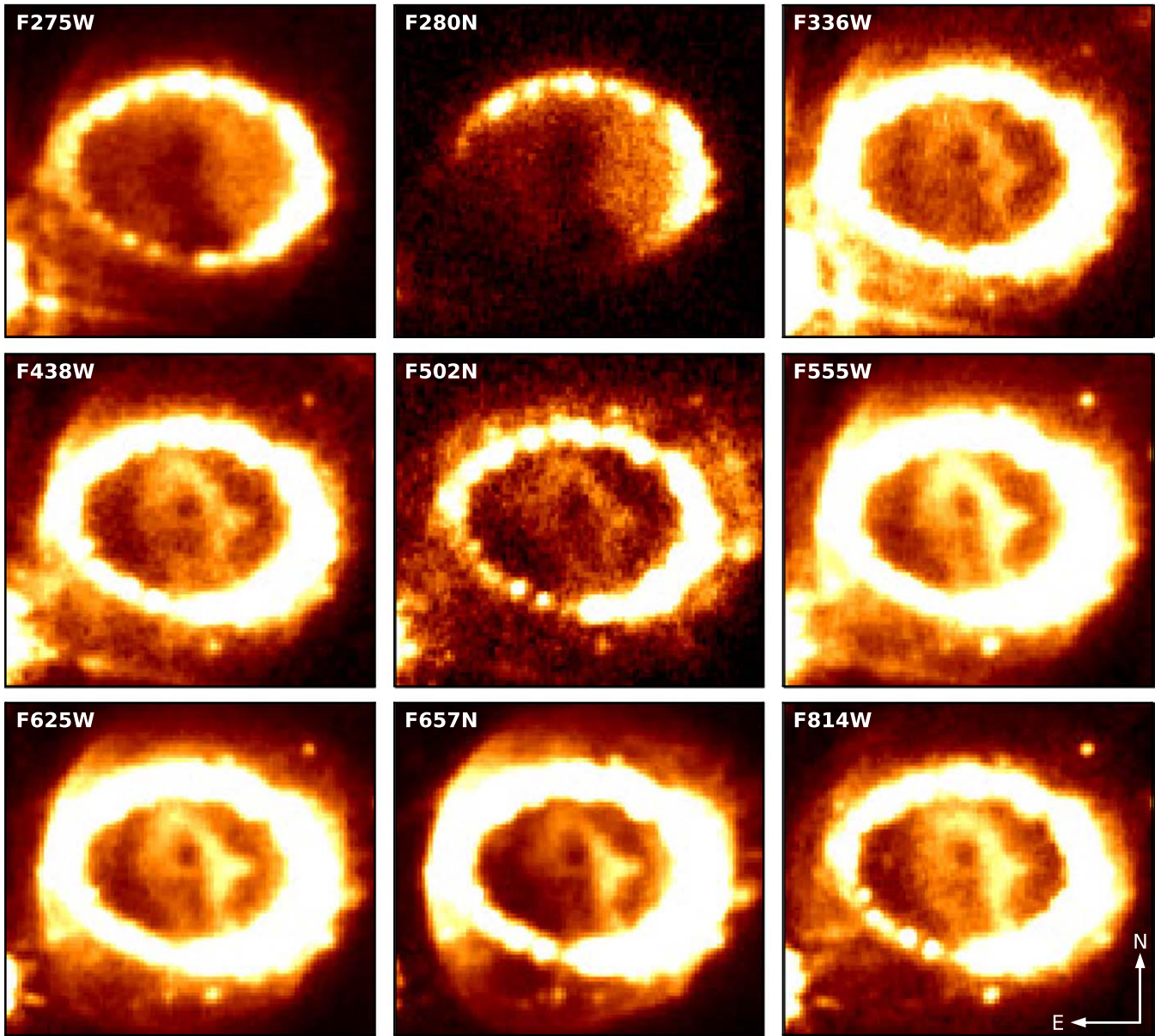
The broadband filters cover many lines that might differ between the ejecta and the ER. Regarding the ejecta, scattering by the Mg II  $\lambda\lambda$  2795, 2802 lines dominates in the F275W filter. The formation of these fluorescent lines is partly powered by Ly $\alpha$ , which is absorbed in the Mg II  $\lambda$  1240 line, which then in turn produces the Mg II  $\lambda\lambda$  2795, 2802 lines (see discussion in Section 7.2; but also Kangas et al. 2022). We here note that the F225W filter used in the 2009 observations mainly contains Fe I, Fe II, and Si I lines (Jerkstrand et al. 2011), while the Mg II lines only slightly contribute to this filter. No single line dominates in the F336W filter, and no clear line identification can be made in the range between 3000 and 3500 Å as asserted by Jerkstrand et al. (2011). Instead, the F336W filter covers a blend of scattering and fluorescence lines, mostly from Fe: The emission is a mix of mainly H I and Fe I-II lines, but also scattering from resonance lines of trace elements in the H envelope. The range covered by the F438W filter is a blend of Fe I, Ca I, H I, notably the Ca I  $\lambda$  4226 emission line, complemented with emission and scattering from the Fe/He zone



**Figure 3.** STIS spectra from 2017 (described in Kangas et al. 2022) of the ER (gray) and the ejecta (black), and HST/WFC3/UVIS2 filters’ response functions (in colors). The spectra were obtained from two adjacent  $0''.2$  wide slits oriented in the north–south direction, covering the central part of the remnant. They were smoothed with the Savitzky–Golay algorithm for visual clarity. Lines contributing to the ejecta and the ER are identified in black and gray, below and above the spectra, respectively.

**Table 3**  
Minimum and Maximum Velocities for the Main Emission Lines of the Ejecta in the Narrowband Filters at 50% and 10% of the Peak Transmission

Filter	Ion	Reference Wavelength ( $\text{\AA}$ )	$v_{\text{min},10\%}$ ( $\text{km s}^{-1}$ )	$v_{\text{min},50\%}$ ( $\text{km s}^{-1}$ )	$v_{\text{max},50\%}$ ( $\text{km s}^{-1}$ )	$v_{\text{max},10\%}$ ( $\text{km s}^{-1}$ )
F280N	Mg II	2799	−3443	−2854	+1643	+2767
F502N	[O III]	5008	−2922	−2097	+1863	+2270
F657N	H $\alpha$	6565	−3518	−3061	+2681	+3685



**Figure 4.** HST/WFC3 images of SN 1987A taken 12,980 days after the explosion in nine different filters. The images were scaled by an asinh function, and the color scales were chosen differently for each filter to highlight the weak emission in the ejecta. The field of view for each image is  $2''.50 \times 2''.25$ .

([Fe II]  $\lambda\lambda$  4223, 4339, 4453), and  $H\gamma$   $\lambda$  4343. The F555W filter is largely dominated by the  $H\beta$  line, although Fe I also contributes to the feature at 4850 Å. The  $H\alpha$  line dominates in the F625W filter, and also contributes to the F555W filter. The [O I]  $\lambda\lambda$  6300, 6364 lines contribute to both the F555W and F625W filters, although their fluxes are contaminated by Fe I lines in this wavelength range. The F814W filter is dominated by the [Ca II]  $\lambda\lambda$  7293, 7326 lines.

The ER has many strong lines that also appear in the ejecta. Additional lines contribute to the different filters (see Figure 3), and we refer the reader to Gröningsson et al. (2008) for a thorough identification of the emission lines from the ER.

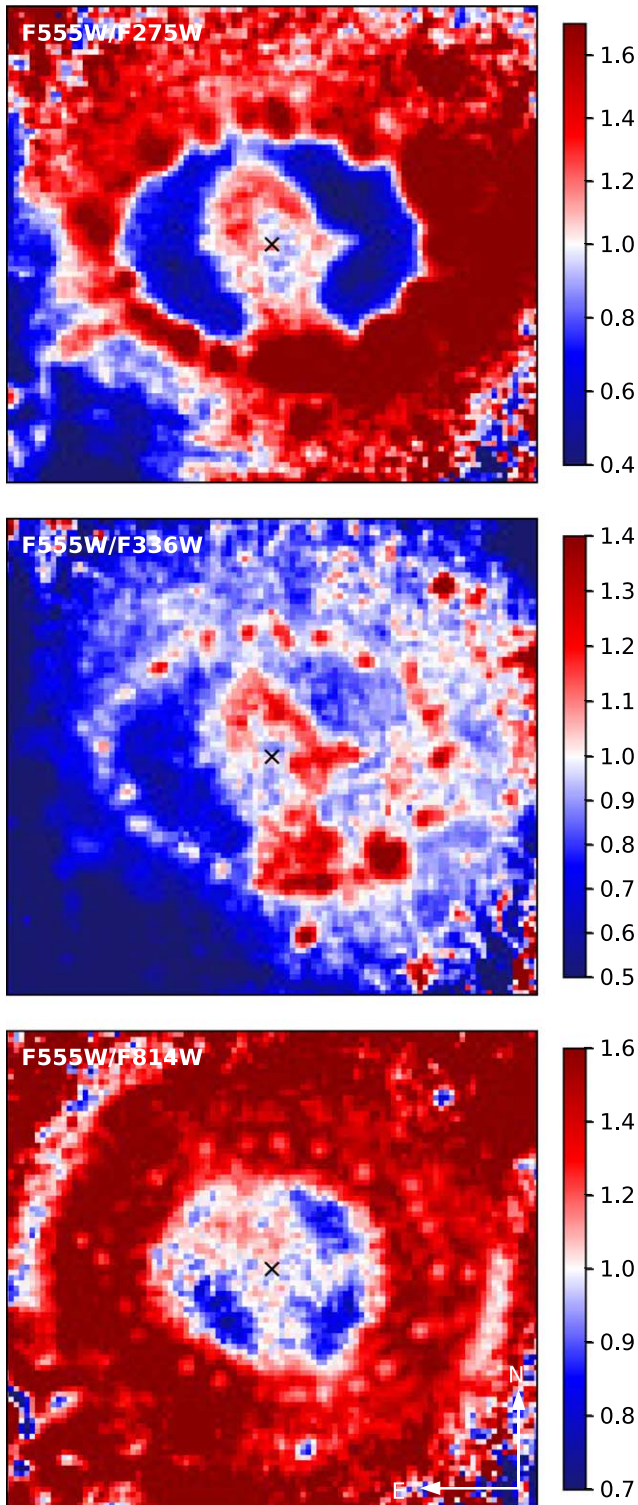
#### 4. Morphology

The HST/WFC3 observations of SN 1987A at day 12,980 after the explosion are presented in Figure 4 and Appendix Figure 14 (optimized to see the ejecta and ER, respectively).

The morphology of the ER at epoch 12,980 days is very similar in all filters: brightest in the west and faintest in the southeast. Part of the ER is missing in the F280N filter due to the narrow filter not covering all Doppler shifts (see Section 3). Emission is observed outside the ER, including the reverse shock (especially in filters with strong H lines) and an outer portion on the west side in the F502N filter. These emission components will be studied in a separate paper.

##### 4.1. Morphologies of the Ejecta at Day 12,980 after the Explosion

Overall, the ejecta appearance is very similar in all filters, with the exception of the Mg II-dominated ones (F275W and F280N). The ejecta show a north–south elongation where it is brightest. The western part of the ejecta appears brighter than the eastern part, while a small dimmer hole, a region actually called “the hole,” located slightly north to the center of the



**Figure 5.** Ratio of HST/WFC3 images of SN 1987A taken 12,980 days after the explosion scaled by the ratio of count rates in the center region (note the two linear scales for values  $\geq 1$  and  $\leq 1$ , respectively). The highest-resolution images were degraded in resolution to match the lowest-resolution images (see main text for details). The field of view for each image is  $2''.50 \times 2''.25$ . The black cross indicates the geometric center of the ejecta.

ejecta, appears. These observations are very similar to the HST observations taken during the last few years (see Appendix A).

Given that Balmer hydrogen lines mostly dominate in the F555W, F625W, and F657N filters, it is not surprising that the

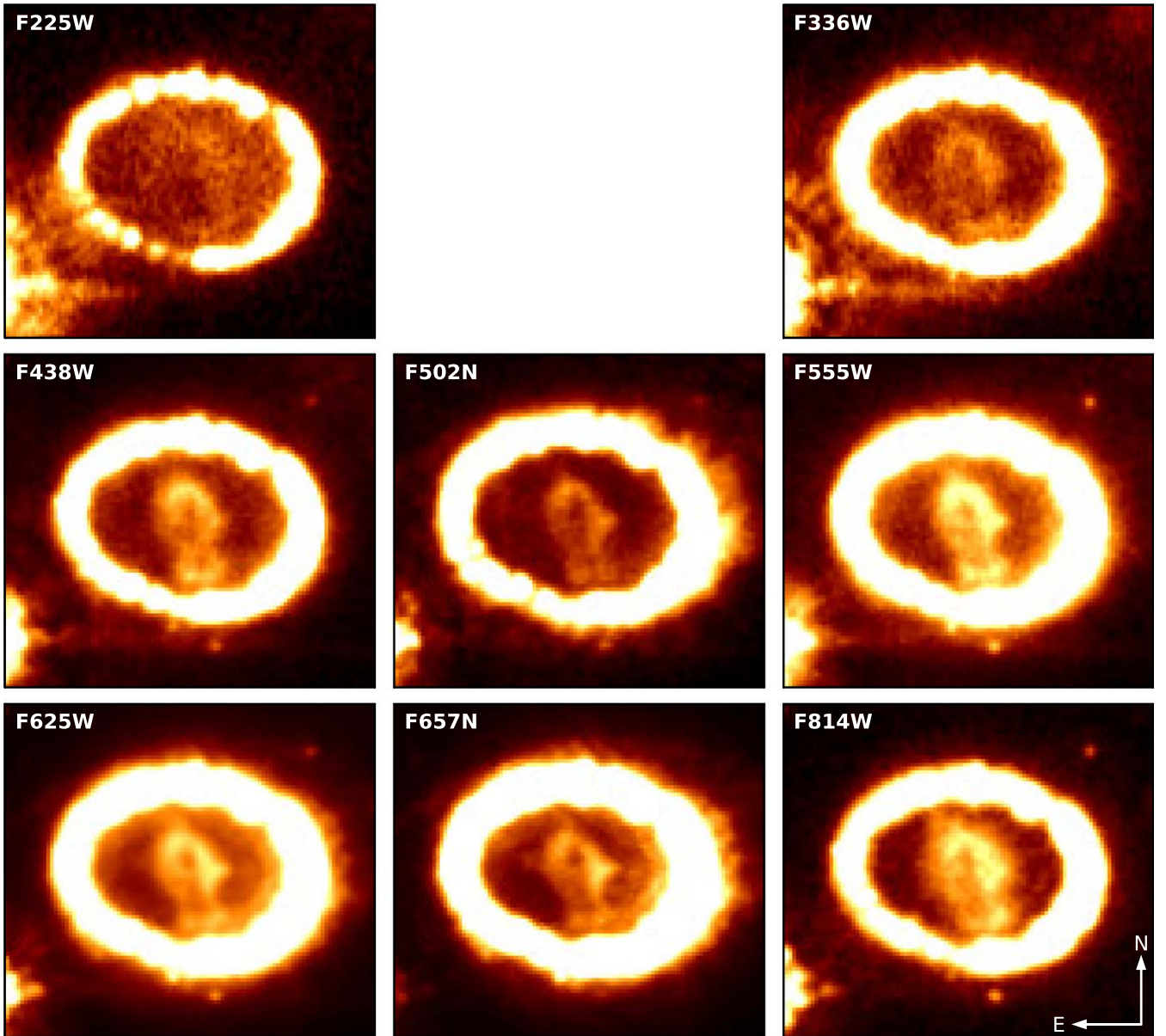
observations taken in these filters are very similar in terms of morphology, although the F657N image looks a little different from the F625W due to the limited filter width (some of the ejecta are Doppler shifted outside, see Section 3). A similar overall morphology is observed in the F336W, F438W, and F814W filters, although it is notable that the S/N in the ejecta is low in the former two filters (see Section 3). The ejecta morphology in the F502N filter is strongly affected by the narrow filter width, which only covers the Fe I line. Finally, the morphology of the ejecta in the F275W and F280N filters differs from the other filters because of Mg II resonance line scattering (discussed in Kangas et al. 2022, based on the STIS spectra), which can occur in both the metal core and the H and He envelopes of the preexplosion progenitor star.

To better identify the differences in morphology between the filters, we investigated the ratio between pairs of images. We accounted for the small wavelength dependence of the spatial resolution (the FWHM varies between  $0''.086$  and  $0''.095$  depending on the filter) by degrading the resolution of the high-resolution image to match the corresponding low-resolution image. We used the `photutils` PSF matching package (with a Hanning window) in `python` and adopted a well-isolated star in the field of view as our reference for the point-spread function (PSF). These matched kernels were convolved with the `python` package `scipy` `ndimage` with a convolution mode “nearest.” We then scaled the image ratios by the corresponding count rates in the center region to better highlight the differences in morphology between the different filters. The main results are presented in Figure 5 and discussed hereafter. We note that this PSF matching is not perfect: some residuals are left in the images, mainly at the locations of the hotspots (see the relative brightness difference between the ER spots’ interior and rim), while the ejecta seem to be free of these artifacts.

Compared to the filter F555W, the region around the inner ejecta but inside the ER is proportionally much brighter in the F275W filter (see upper panel of Figure 5), especially in the western part. The central region of the ejecta is also proportionally slightly brighter than the rest of the ejecta in the F275W filter compared to the F555W filter. The spots, especially the southwestern ones, in the F275W are proportionally fainter. A slight relative difference in brightness is observed between the filters F336W and F555W: The region east (respectively west) of the ejecta but inside the ER is proportionally slightly brighter (respectively fainter) in the F336W filter, highlighting the shape of the ejecta (see middle panel in Figure 5). The ejecta are proportionally brighter than the ER in the F814W filter compared to the F555W filter (see lower panel in Figure 5). From the overall similarity, we infer the ejecta are chemically well mixed on large scales.

#### 4.2. Evolution of Morphologies of the Ejecta between Days 8329 and 12,980 after the Explosion

The HST/WFC3 observations of SN 1987A at day 8329 after the explosion are presented in Figure 6 and Appendix Figure 15 (optimized to see the ejecta and ER, respectively). We refer to Larsson et al. (2013) for a thorough analysis of these observations. We compare the morphologies of the HST observations taken at day 12,980 to those taken at day 8329 in the seven common filters, namely F336W, F438W, F502N, F555W, F625W, F657N, and F814W, assuming the ejecta were expanding freely at constant velocity following Equation (1). To this aim, the observations at day 12,980 were resampled by a factor of 1.56,



**Figure 6.** HST/WFC3 images of SN 1987A taken 8329 days after the explosion in eight different filters. The images were scaled by an asinh function, and the color scales were chosen differently for each filter to highlight the weak emission in the ejecta. The scales are twice as large as those of the corresponding 2022 images (see Figure 4). The field of view for each image is  $2''.50 \times 2''.25$ .

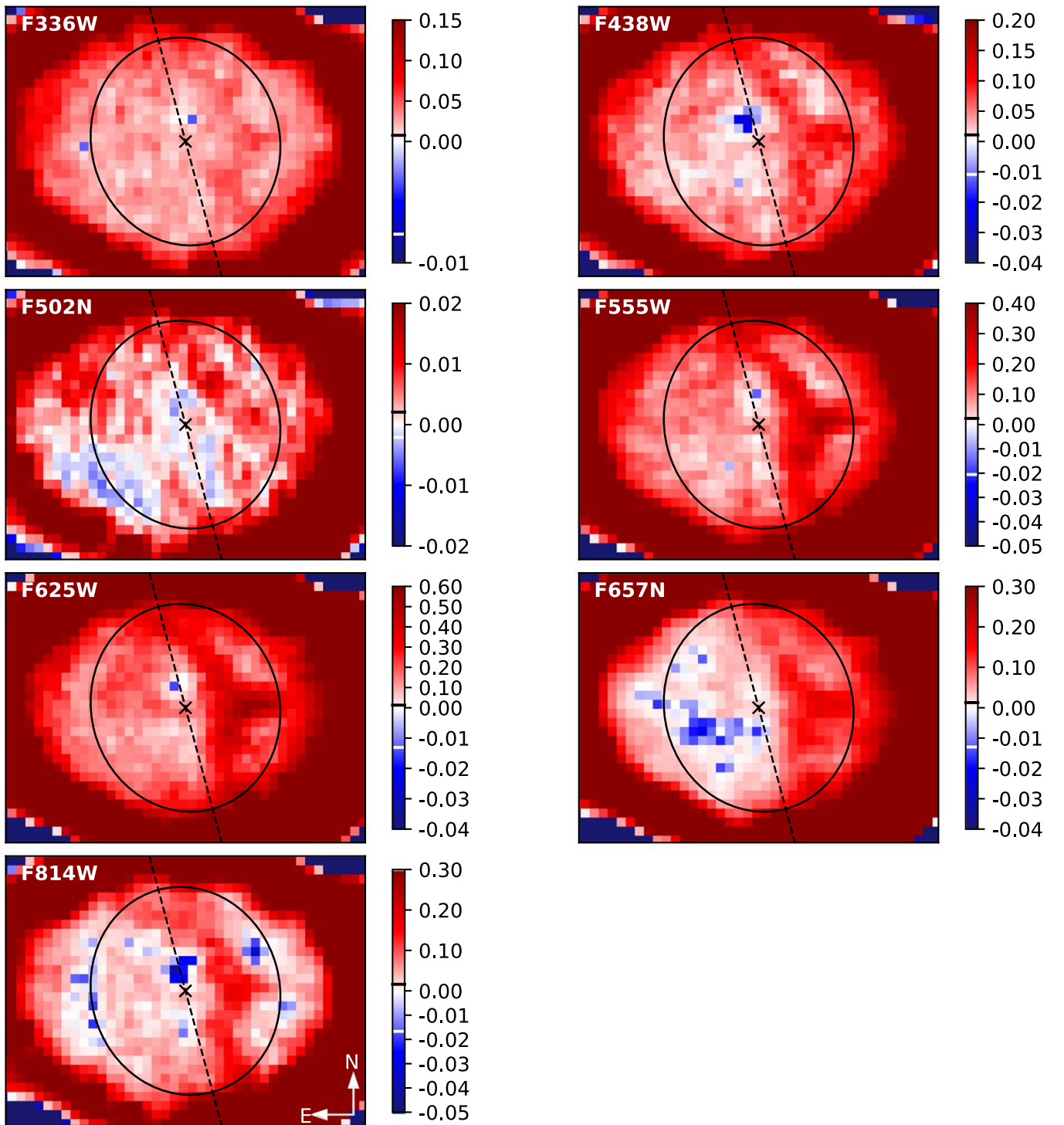
corresponding to the ratio between the number of days after the explosion of the two epochs of observations. In practice, we drizzled the dithered exposures assuming a pixel size 1.56 times larger than the pixel size of  $0''.025$  adopted in the rest of the paper (see Section 2); all other parameters are identical. As such, it is as if the epoch 12,980 observations were run backwards in time and “reobserved” at epoch 8329. In this process, the resulting images have the same number of pixels in the region covering SN 1987A.

We then subtracted the observations at day 8329 from the corresponding reduced observations at day 12,980, the results of which are presented in Figure 7. We multiplied the images by a scale factor to account for the small (maximum 2%) decrease in instrumental sensitivity between the observations. Other changes related to the performance of WFC3 are handled in the data reduction process. We here note that only the region of the ejecta is relevant in this context, as the ER in the more recent observations was artificially reduced in size in the

process and therefore does not have any physical meaning.<sup>11</sup> The images indicate dimming in “the hole” just above the central region in all filters, although it is significant at the  $3\sigma$  level only in filters F438W, F502N, and F814W. In all filters, we observe a clear brightening of the west part of the inner ejecta compared to the rest of the inner ejecta. These two features point toward the presence of an external source of energy powering the ejecta in addition to the radioactive decay of  $^{44}\text{Ti}$ , as no such structure would clearly stand out if radioactivity was the main source of energy powering the freely expanding ejecta (see discussion in Section 7.1).

<sup>11</sup> We could rather expand the 2009 images by the same 1.56 factor. However, in that case, rather than reducing the resolution of the ejecta in the 2022 images to the 2009 level, we would artificially increase the resolution of the 2009 images to the 2022 level.





**Figure 7.** Differences of SN 1987A HST/WFC3 images between epochs 12,980 and 8329 days after the explosion in the seven common filters. The observations at day 12,980 were reduced in size and “reobserved” at the epoch of the observations at day 8329 assuming the ejecta were expanding freely, before subtraction in order to highlight the change of morphology in the ejecta. To account for the changing ER contribution to the ejecta, an offset of  $-0.0063$ ,  $-0.0083$ ,  $-0.0016$ ,  $-0.0196$ ,  $-0.0319$ ,  $-0.0230$ , and  $-0.0097$ , respectively (corresponding to the mean flux of the ER inside the ejecta as computed from the synthetic models for the ER, see Appendix B), was applied to the images. The aperture defining the ejecta region is overlotted on the images as a black ellipse. The dashed line represents the separation between the eastern and western parts. The field of view for each of the images is  $0''.500 \times 0''.375$ . Values are given in units of electrons per seconds (note the two different, but linear, intensity scales for positive and negative values, with 0.0 as the crossover point). The black and white lines in the colorbars indicate the  $3\sigma$  levels above and below which differences are significant, calculated from the number of counts in individual pixels in the ejecta region.

## 5. Broadband and Narrowband Photometry

In this section, we analyze the broadband and narrowband photometry in the three different regions presented in Figure 2, namely the ER, the ejecta, and the center in the different filters in

the observations taken at epoch 12,980 and compare them to the observations at epoch 8329. All regions are centered on the SN geometric center ( $\alpha = 05^{\text{h}}35^{\text{m}}27^{\text{s}}.9875$ ,  $\delta = -69^{\circ}16'11''.107$ , Alp et al. 2018).

**Table 4**  
Dereddened Flux Measurements in the ER, Ejecta, and Center at Epoch 12,980 in All Nine Filters

Filter	ER Flux ( $10^{-15}$ erg cm $^{-2}$ s $^{-1}$ Å $^{-1}$ )	Ejecta Flux ( $10^{-16}$ erg cm $^{-2}$ s $^{-1}$ Å $^{-1}$ )	Center Flux ( $10^{-17}$ erg cm $^{-2}$ s $^{-1}$ Å $^{-1}$ )
F275W	2.614 ± 0.003	4.136 ± 0.013	2.594 ± 0.031
F280N	7.194 ± 0.015	15.067 ± 0.070	8.280 ± 0.165
F336W	1.370 ± 0.001	1.060 ± 0.004	0.749 ± 0.010
F438W	1.229 ± 0.001	1.075 ± 0.004	0.725 ± 0.010
F502N	0.768 ± 0.001	0.744 ± 0.004	0.464 ± 0.009
F555W	0.772 ± 0.001	0.621 ± 0.001	0.450 ± 0.004
F625W	1.117 ± 0.001	0.784 ± 0.002	0.573 ± 0.004
F657N	6.879 ± 0.003	3.030 ± 0.007	2.234 ± 0.018
F814W	0.237 ± 0.001	0.290 ± 0.001	0.203 ± 0.002

**Table 5**  
Dereddened Flux Measurements in the ER, Ejecta, and Center at Epoch 8329 in All Eight Filters

Filter	ER Flux ( $10^{-15}$ erg cm $^{-2}$ s $^{-1}$ Å $^{-1}$ )	Ejecta Flux ( $10^{-16}$ erg cm $^{-2}$ s $^{-1}$ Å $^{-1}$ )	Center Flux ( $10^{-17}$ erg cm $^{-2}$ s $^{-1}$ Å $^{-1}$ )
F225W	7.402 ± 0.015	4.236 ± 0.037	3.166 ± 0.101
F336W	2.790 ± 0.003	0.809 ± 0.006	0.641 ± 0.017
F438W	2.418 ± 0.002	0.915 ± 0.004	0.692 ± 0.012
F502N	2.402 ± 0.002	0.667 ± 0.003	0.479 ± 0.009
F555W	1.614 ± 0.001	0.511 ± 0.002	0.411 ± 0.006
F625W	2.377 ± 0.001	0.611 ± 0.001	0.509 ± 0.002
F657N	17.144 ± 0.006	2.665 ± 0.008	2.286 ± 0.024
F814W	0.488 ± 0.001	0.261 ± 0.001	0.200 ± 0.003

The flux in the ER was computed assuming the same elliptical annulus for all observations, that is to say, assuming the expansion velocity of the ER is negligible.<sup>12</sup> The region was chosen to be sufficiently large to encompass the bright emission seen in all observations, and is represented by the dotted cyan lines in Figure 2. The annulus has an aspect ratio of 0.73, a position angle of 173°, and its internal and external major axes equal to 1''21 and 2''18, respectively.

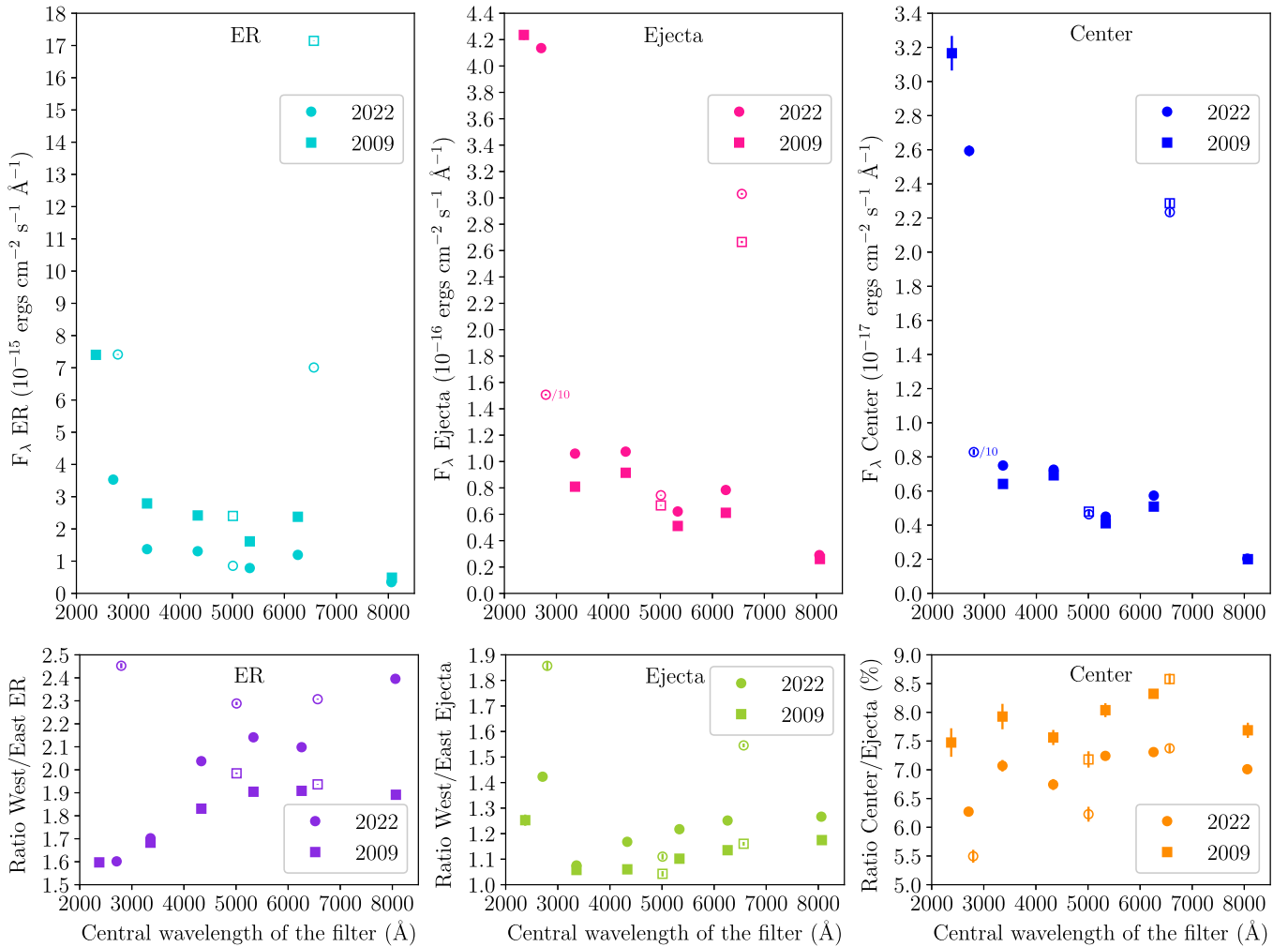
The flux in the ejecta was computed in an elliptical region defined by a major axis corresponding to an ejecta speed of 3000 km s $^{-1}$ , an aspect ratio of 0.90, and a position angle of 105° (Larsson et al. 2011), as depicted by the dashed cyan line in Figure 2. The fluxes reported for the ejecta region throughout the paper include all of the flux inside the elliptic aperture schematized in Figure 2, and thus include the flux in the center too. This size of the ejecta region allows us to capture most of the bright inner ejecta, while avoiding the ER. The flux in the center was computed in a circular region defined by a radius corresponding to an ejecta speed of 800 km s $^{-1}$ , as depicted by the cyan solid line in Figure 2. The motivation for looking at this specific region is that it should cover the compact object, considering a plausible range of kick velocities (Alp et al. 2018; Fransson et al. 2024). We here point out that defining the regions in terms of expansion velocity means that they are smaller (in arcseconds) in the observations taken at epoch 8329 according to Equation (1), as notably shown in Appendix A.

<sup>12</sup> The expansion velocity of the ER was measured in Larsson et al. (2019a): The semimajor axis expands at  $680 \pm 50$  km s $^{-1}$ , corresponding to 3 mas yr $^{-1}$ , that is to say, 0.12 pixels per year. Over the 12.73 yr from day 8329 to 12,980, this would total to 1.5 pixels of expansion. This number of pixels is negligible compared to our adopted aperture, which is large enough to accommodate a 1.5 pixels expansion from day 8329 through all epochs up to day 12,980.

We summed the count rates over the pixels inside the given regions, accounting for fractional pixels. The  $1\sigma$  statistical uncertainties are nonnegligible (and bigger than the plot symbols) only in the center region. The count rates were converted into fluxes using the inverse sensitivity of the filters. Finally, the fluxes were dereddened adopting a Milky Way extinction curve of Cardelli et al. (1989) with a color excess  $E(B - V) = 0.19$  mag, and a reddening factor in the  $V$ -filter  $R_V = 3.1$ , as suggested by France et al. (2011).

The regions encompassing the ejecta, and, to a lesser extent, the center, are contaminated by scattered ER emission. Given that we cannot separate the ER contribution from the ejecta and center contributions based on the images, we had to rely on a synthetic model of the ER (see Appendix B) to remove the contribution of the ER to the ejecta and center. It led to a reduction of the ejecta and center fluxes by 6.3% to 20.8%, depending on the date of observation and filter (see Table 7 in Appendix B). The ER contribution to the ejecta and center does not change much with time because the fading of the ER and the expanding ejecta and center apertures affect this level in opposite directions.

We additionally note that our line of sight from Earth places the southern rim of the northern outer ring in projection behind the center of the ejecta, adding to its flux. This contribution cannot easily be removed due to the spatial variations of the brightness of the outer rings. However, we used the faintest and brightest parts of the northern outer ring outside the ER to place limits on the contribution of the northern outer ring (Appendix C). The contributions are  $\lesssim 5\%$  in the ejecta region and  $\lesssim 15\%$  in the center region for most filters, typically changing by  $\lesssim 3\%$  between the epochs. The largest contributions by far are seen in the F502N filter, where it reaches



**Figure 8.** Broadband and narrowband photometry of the ER (top left panel), ejecta (top middle panel), and center (top right panel). Corresponding ratios between western and eastern parts in the ER (bottom left panel) and ejecta (bottom middle panel), and ratio between the center and full ejecta fluxes (bottom right panel). The observations at epochs 12,980 and 8329 (labeled 2022 and 2009, respectively) are marked with circles and squares, respectively, while broadband and narrowband filters are shown with filled and open symbols, respectively. We note that the error bars are smaller than the symbols in most cases. Since the shortest wavelength filters are different in the two epochs, they are plotted side by side and not included in Figure 9.

maximal levels of 46% and 25% in the center region at epochs 12,980 and 8329, respectively (see Table 9 in Appendix C).

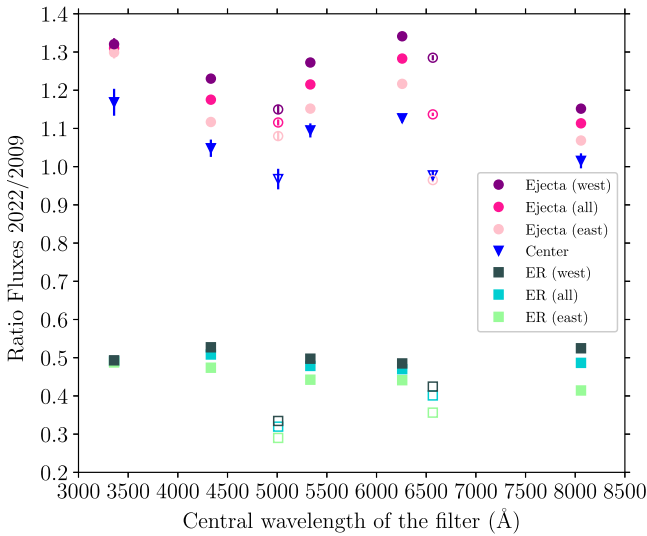
Given that the X-ray input from the ER to the ejecta is not uniform and especially presents an east–west asymmetry (Frank et al. 2016), it is interesting to investigate the asymmetries between the east and west parts of both the ER and ejecta in the HST data. In order to quantify differences between the east and west regions seen in the images (see Section 4), we separated the ejecta and ER regions into east and west parts, the boundary separating the two parts being the major axis of the ellipse encompassing the ejecta region (dashed line in Figure 2). We then proceeded as for the full regions to compute the fluxes in the east and west parts.

The photometry of the full regions at epochs 12,980 and 8329 is provided in Tables 4 and 5, and presented in Figure 8 together with the ratio between the western and eastern parts for the ER and ejecta, as well as the ratio between the center and ejecta. The ratios between the fluxes at epochs 12,980 and 8329 are presented in Figure 9 for the ER, ejecta, and center regions, as well as the eastern and western parts of the ER and ejecta. Since the shortest wavelength filters are different in the

two epochs, they are plotted side by side in Figure 8 and not included in Figure 9.

The ER is overall dimmer by a factor of 2 at epoch 12,980 compared to epoch 8329, with the dimming more pronounced in the narrowband filters. The eastern part has dimmed more than the western part (except in the F336W filter where no difference is observed between east and west).

The ejecta have brightened by  $\sim 20\%$  between the two epochs, the largest increases being observed in the F336W and F625W filters. The photometry of the ejecta shows more variations as a function of wavelength than the one of the ER. Overall, the western part of the ejecta has brightened more than the eastern part, except in the F336W filter where no noticeable difference is observed, and except the eastern part in the F657N filter that has slightly dimmed. The center region has brightened in the broadband filters, less than in the ejecta region, but has not changed significantly in the narrowband filters. The photometry of the center is very similar to the photometry of the ejecta (with small variations seen in the bottom right panel of Figure 8) and has evolved similarly with time as the photometry of the ejecta.



**Figure 9.** Ratio between the fluxes at epochs 12,980 and 8329 for the seven common filters in the ER (full region and western and eastern parts), ejecta (full region and western and eastern parts), and center. Broadband and narrowband filters are shown with filled and open symbols, respectively.

The full luminosity of the ER, ejecta, and center in the UV-optical band covered by the HST broadband filters amount to  $(5.75 \pm 0.01) \times 10^{35}$ ,  $(5.69 \pm 0.02) \times 10^{34}$ , and  $(3.88 \pm 0.04) \times 10^{33}$  in 2022, and  $(1.183 \pm 0.001) \times 10^{36}$ ,  $(4.47 \pm 0.02) \times 10^{34}$ , and  $(3.49 \pm 0.07) \times 10^{33}$  erg s<sup>-1</sup> in 2009, respectively. These luminosities were computed based on the FWHM of the filters and corresponding fluxes in these filters. Although the filters overlap over certain wavelength ranges, they do so where the ejecta spectrum is free of any dominant line (see Figure 3), so our determination of the total luminosities should not be affected by these overlaps.

## 6. Light Curves

This section is devoted to the analysis of the light curves of the ER, ejecta, and center of SN 1987A in the two filters, F438W and F625W, that are common to all 12 epochs from day 8329 to day 12,980, and is a major update from Larsson et al. (2019a). The fluxes were computed as described in Section 5. The observations in the F438W and F625W filters are shown in Figure 10 and Appendix A, Appendix Figure 16 (optimized to see the ejecta) together with the adopted ejecta and center regions, and Appendix Figure 17 (optimized to see the ER). Both ejecta and center regions are expanded linearly with time for the assumed homologous expansion of the ejecta following Equation (1). The ejecta region clearly misses the bright southern part of the ejecta, but we cannot make it bigger due to the overlap with the ER in recent years. A direct quantitative comparison of the fluxes to previous works is impossible as we adopted a smaller region size for the ejecta to encompass most of the ejecta in the latest observations while avoiding the ER.

Depending on the orientation of the telescope at the time of the observation, diffraction spikes from Stars 2 and 3 might cross the center, ejecta, or ER regions.<sup>13</sup> The extra contribution of the diffraction spikes to the flux in the corresponding region was subtracted as described in Appendix D. This correction is

<sup>13</sup> The observations at epochs 8329 and 12,980 were not affected by diffraction spikes from Stars 2 and 3.

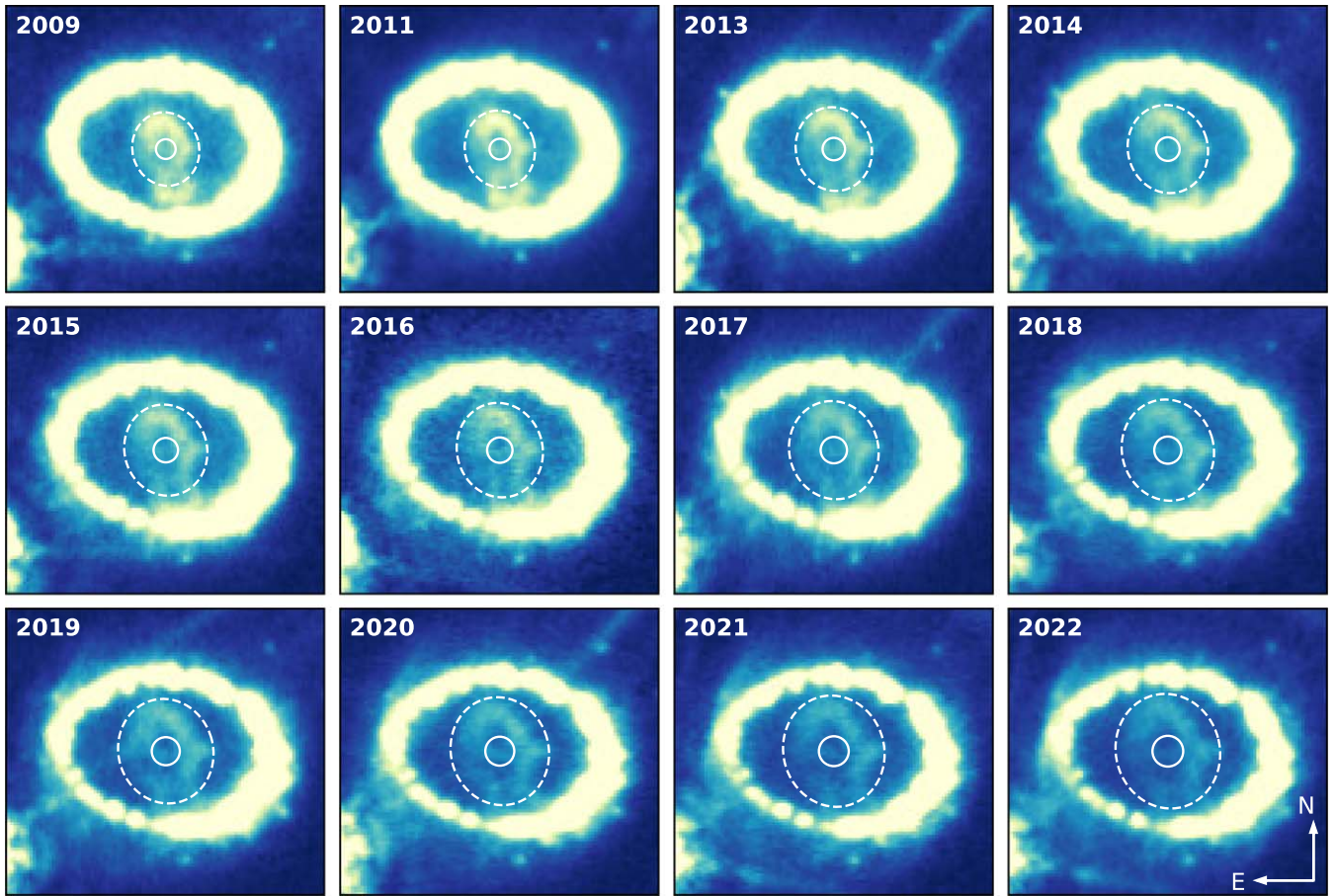
at the level of 4% at most. We also modeled and removed the contribution of the scattered light from the ER to the ejecta and the center, as explained in Appendix B. The contribution of the northern outer ring to the ejecta and center (see Figure 1) amounts to 0%–7% and 1%–17% in the F438W filter and 1%–4% and 3%–10% in the F625W filter (estimated as described in Section 5 and Appendix C), respectively.

The flux measurements in the ER, the ejecta, and the center between epochs 8717 and 12,598 in the F438W and F625W filters are provided in Table 6. The light curves are presented in the three panels of Figure 11 for the ER, ejecta, and center together with the ratio between the western and eastern parts for the ER and ejecta and the ratio between the center and the ejecta. Light curves for the ER and ejecta extending to earlier epochs are presented in Larsson et al. (2019a, their Figures 10 and 11). The exact flux values are not directly comparable with this work due to the abovementioned small differences in apertures, and the fact that correction factors were applied to the light curves in Larsson et al. (2019a) to account for the differences between the three different instruments used (Wide Field Planetary Camera 2, Advanced Camera for Surveys, and Wide Field Camera 3). However, the general time evolution is not affected by these differences, and follows a similar trend in both works, therefore enforcing that adopting different apertures does not change the results qualitatively.

The decline in the light curve of the ER is explained by the fading of the hotspots that started  $\sim 8000$  days after the explosion (Fransson et al. 2015). The fading of the hotspots is interpreted as the forward shock (with light-travel delays) reaching the full circumference of the ER, such that no new hotspots were appearing, and the older hotspots fading as they were destroyed by the shock. In both filters, the ratio between the fluxes in the western and eastern parts of the ER increased until day  $\sim 11,500$ , after which it decreased. This indicates that the eastern part has proportionally faded more and more compared to the western part until day  $\sim 11,500$ , after which the fading rate of the western part started to catch up with that of the eastern part. This could be due to the increasing contribution of the reverse shock emission in the east, which falls inside the defined aperture for the ER.

An increase in the ejecta flux is observed until days  $\sim 10,700$  (F438W) and  $\sim 11,100$  (F625W), after which the flux flattens at a constant value. The ratio between the fluxes in the western and eastern parts of the ejecta in the F625W and F438W filters follows the increase observed in the total flux in the corresponding filter until day  $\sim 11,100$ , after which it drops to values of 1.25 and 1.16, respectively. This shows that most of the brightening between epochs 8329 and 12,980 occurred before  $\sim 10,700$  days. The small, although noticeable, increase in the ejecta flux in the two filters at day 12,200, as well as the drop at the same date in the ratio between the fluxes in the western and eastern parts of the ejecta in the F438W filter, are unlikely to have any astrophysical origin but are rather due to an improper diffraction spike contribution estimate. Indeed, this level of variability on a 1 yr timescale is unlikely to be real. The color of the ejecta, determined from the flux ratio between the F625W and F438W filters, has stayed roughly constant (values between 0.66 and 0.72 in unitless ratios) between days 8329 and 12,980, therefore supporting that the energy source and physical conditions have not changed in this time interval.

The light curve of the center region shows a clear increase across the first three epochs, followed by a general flattening



**Figure 10.** HST/WFC3 images showing the evolution of SN 1987A in the F438W filter between epochs 8329 and 12,980 (labeled by the year of observation). The emission in the lower left corner is due to Star 3 (see Figure 1). The images were scaled by an asinh function to highlight the weak emission in the ejecta. The field of view for each image is  $2''.50 \times 2''.25$ . The white circle and dashed white ellipse overlotted on each image represent the center and ejecta regions, respectively, adopted to compute the fluxes. These regions grow in size from 2009 to 2022, using Equation (1) to define a comoving volume that tracks the same expanding ejecta with time.

after day  $\sim 10,000$  (see Figure 11). The ratio between center and ejecta fluxes has overall decreased with time, highlighting the increasing flux in the outer part of the ejecta (as best seen in Figure 7), pointing toward an external source of energy powering the outer parts of the inner ejecta in addition to the  $^{44}\text{Ti}$  radioactivity, notably X-rays from the ER.

## 7. Discussion

SN 1987A is the only modern SN for which the time evolution of the ejecta can be studied with spatial resolution—providing information about the evolving physical conditions and revealing the explosion geometry in increasingly great detail. For the range of epochs considered in this paper (from day 8329 to 12,980 after the explosion), the ejecta have expanded by a factor of 1.56, allowing us to resolve correspondingly smaller spatial scales. The observed ejecta morphology is strongly affected by the various time-evolving energy sources, so we start by discussing them in Section 7.1, followed by a discussion of the line excitation mechanisms and their connection to the ejecta morphology in Section 7.2. We then discuss the intrinsic, asymmetric distribution of the ejecta in Section 7.3, and finally consider the implications of the nondetection of the compact object in the HST images in Section 7.4.

### 7.1. Energy Sources in the Ejecta

A previous analysis of the ejecta light curve from HST imaging showed that the ejecta faded as expected from the decay of  $^{44}\text{Ti}$  until  $\sim 5000$  days, after which it started brightening. Modeling showed that the brightening is consistent with energy input from X-rays originating from the ER (Larsson et al. 2011; Fransson et al. 2013). The flux more than doubled in all filters covering the 2000–11000 Å wavelength range by day 8329 (Larsson et al. 2011; Larsson et al. 2013), clearly making X-rays the dominant energy source at late times. The fluxes measured in the F625W and F438W filters subsequently continued to increase, but at a gradually lower rate, showing signs of levelling off at day  $\sim 11,000$  (Larsson et al. 2019a). Here, we have added four more epochs of data compared to Larsson et al. (2019a), which confirm the flattening of the light curves and show that the ejecta flux has remained approximately constant since  $\sim 11,000$  days (see Figure 11, middle). Considering the full wavelength range, the brightening between days 8329 and 12,980 is  $\sim 20\%$  (see Figure 9).

Figure 12 shows the HST light curves of the ejecta and ER in the F625W filter together with light curves of the X-ray emission from the ER in different energy bands from XMM-Newton observations (Alp et al. 2018; Maitra et al. 2022). The soft X-ray (0.5–2 keV) light curve started decreasing after day

**Table 6**  
Dereddened Flux Measurements in the ER, Ejecta, and Center between Epochs 8717 and 12,598 in the F438W and F625W Filters

Epoch (days)	ER Flux ( $10^{-15}$ erg cm $^{-2}$ s $^{-1}$ Å $^{-1}$ )	Ejecta Flux ( $10^{-16}$ erg cm $^{-2}$ s $^{-1}$ Å $^{-1}$ )	Center Flux ( $10^{-18}$ erg cm $^{-2}$ s $^{-1}$ Å $^{-1}$ )
Filter F438W			
8717	2.417 ± 0.002	0.958 ± 0.003	7.179 ± 0.090
9480	2.249 ± 0.002	1.015 ± 0.004	7.665 ± 0.101
9974	2.115 ± 0.002	1.041 ± 0.004	7.638 ± 0.101
10,317	2.026 ± 0.002	1.056 ± 0.004	7.561 ± 0.101
10,698	1.922 ± 0.002	1.096 ± 0.005	8.071 ± 0.147
11,119	1.749 ± 0.001	1.093 ± 0.004	7.874 ± 0.095
11,458	1.667 ± 0.001	1.065 ± 0.004	7.679 ± 0.101
11,837	1.534 ± 0.001	1.078 ± 0.004	7.907 ± 0.103
12,218	1.411 ± 0.001	1.099 ± 0.004	7.857 ± 0.104
12,598	1.282 ± 0.001	1.076 ± 0.004	7.387 ± 0.099
Filter F625W			
8717	2.286 ± 0.001	0.650 ± 0.001	5.372 ± 0.038
9480	2.073 ± 0.001	0.707 ± 0.001	5.836 ± 0.039
9974	1.942 ± 0.001	0.726 ± 0.001	5.910 ± 0.039
10,317	1.854 ± 0.001	0.743 ± 0.001	5.968 ± 0.039
10,698	1.761 ± 0.001	0.770 ± 0.002	6.198 ± 0.056
11,119	1.609 ± 0.001	0.782 ± 0.001	6.102 ± 0.040
11,458	1.525 ± 0.001	0.770 ± 0.001	5.967 ± 0.039
11,837	1.393 ± 0.001	0.767 ± 0.001	5.890 ± 0.039
12,218	1.280 ± 0.001	0.785 ± 0.001	6.098 ± 0.040
12,598	1.191 ± 0.001	0.779 ± 0.002	5.737 ± 0.041

~10,000, while the hard X-ray (3–8 keV) light curve shows signs of flattening around day ~12,000. These transitions in the X-ray light curves occur around the same epoch as when the optical light curves of the ejecta start flattening.

However, a one-to-one relation between X-rays from the ER and optical ejecta emission is not expected, considering that the flux evolution of the ejecta is affected by the light-travel time between the relative positions of the expanding ejecta and the X-ray emission in 3D, by the decreasing ejecta density, as well as by the evolving shape of the X-ray spectrum (Fransson et al. 2013).

The energy input from the X-rays also affects the observed UV-optical morphology of the ejecta. This is most clearly seen from the fact that the western part of the ejecta has brightened more than the eastern part between days 8329 and 12,980 (see Figure 7), the total optical flux in the western part being a factor of 1.2 brighter in the latest epoch (Figure 8, lower middle panel). This is compatible with the fact that the western part of the ER is brighter than the eastern part by ~1.6 in the X-rays at 10,433 days after the explosion, resulting in more energy being deposited in the western ejecta (see Figure 6 in Frank et al. 2016).

In addition to affecting the west/east flux ratios, the X-ray input leads to a limb-brightened morphology of the ejecta. Most of the X-rays are expected to be absorbed in the outer part of the inner ejecta (the edge-brightened region seen in Figure 4), given the increase in metallicity and the steepening of the density gradient at the boundary of the ejecta core (see models in Fransson et al. 2013). This is supported by our observations, which show that the central region of the ejecta has brightened less than the ejecta as a whole, and even decreased in brightness in the narrowband filters (see Figure 9). In summary, the light curves, east/west asymmetry, and limb-brightened morphology all support the general scenario that X-rays from the ER dominate the energy input to the ejecta. By

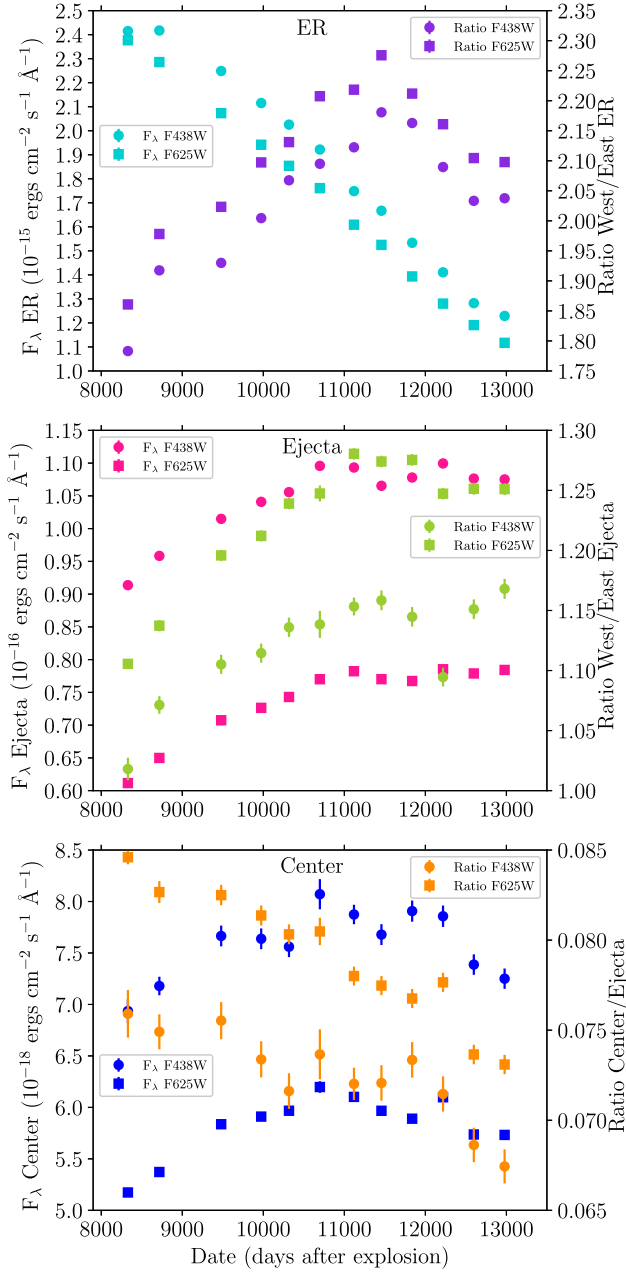
contrast, the energy input from  $^{44}\text{Ti}$  is instead expected to result in a gradual fading without significant spatial variations.

The only part of the ejecta where  $^{44}\text{Ti}$  may still dominate is the innermost region. Indeed, the “hole” in the ejecta located just north of the center (e.g., Larsson et al. 2011; Larsson et al. 2013) is still clearly visible (see, e.g., Figure 4), and Figure 7 indicates that it has faded between epochs 8329 and 12,980 in almost all filters. To quantify the possible fading of the hole, we integrated the flux over a region as large as the region adopted for the center, but centered at the middle of the hole rather than at the center of the ER. We found that the flux decreased by ~7% in the filters that show a clear dimming of the hole (see Section 4.2). Contamination in the hole region by the bright surrounding ejecta is likely nonnegligible, especially in the smaller region at day 8329, and might therefore impact our determination of the flux. Nevertheless, it is interesting to compare these results with the fading expected between these epochs for a region of ejecta powered only by  $^{44}\text{Ti}$  radioactivity,

$$\Delta = \left(1 - \exp\left(\frac{t_2 - t_1}{\tau}\right)\right) \left(\frac{t_1}{t_2}\right)^2, \quad (2)$$

which is 7% for the bolometric flux between  $t_1 = 8329$  days and  $t_2 = 12,980$  days, assuming a linear expansion and a mean lifetime  $\tau$  of 85 yr. Without the IR fluxes, the bolometric flux cannot be computed, but the evolution of the HST fluxes is compatible with the interpretation that  $^{44}\text{Ti}$  dominates over the X-ray input in the “hole”.

Finally, the interpretation of the flux evolution in the central ejecta is further complicated by a large amount of dust, the detailed properties of which are uncertain (see, e.g., Matsuura et al. 2022). An important consideration regarding the dust is that the optical depth is expected to decrease as the inverse of

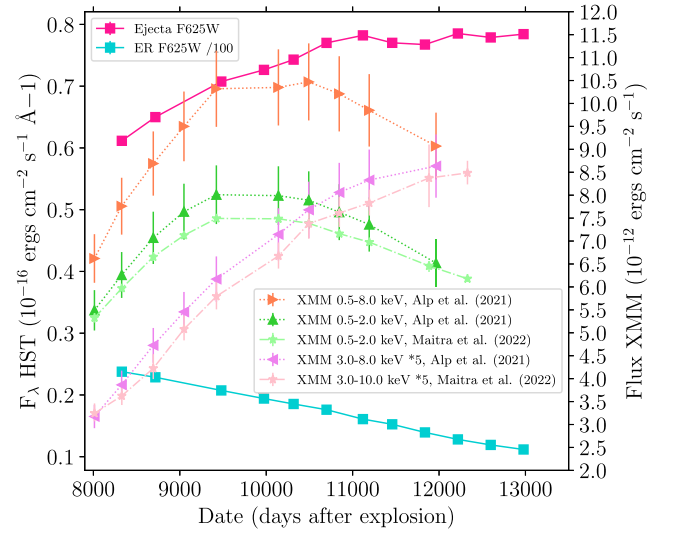


**Figure 11.** Top panel: Light curve of the ER and ratio between west and east parts. Middle panel: Same for the ejecta. Bottom panel: Light curve of the center and ratio between center and ejecta fluxes. We note that the error bars are smaller than the symbols in most cases.

the time squared. The fact that we do not observe any strong brightening in the central region points toward dust still highly optically thick.

### 7.2. Line Excitation and Connection to the Morphology

The X-rays coming from the ER are thermalized, which means that their photoabsorption generates free electrons that ionize and excite atoms in the ejecta. The hydrogen and iron-like emission lines are then produced by recombination. This process results in a similar flux increase in the ejecta and west/east ratio in many of the broadband filters (see Figures 4 and 8). Two notable differences stand out from this picture: (1) the [Ca II] lines contributing to the F814W filter show a smaller increase in flux, and (2) the Mg II lines contributing to the UV



**Figure 12.** X-ray light curves of the ER from XMM-Newton in different energy bands taken from Alp et al. (2021) and Maitra et al. (2022) together with the light curves of the ER and the ejecta in the F625W filter. Some light curves were scaled by a factor of 5 for clarity purposes (see legend).

filters show a high increase in flux and also a very different morphology compared to the other filters.

The smaller increase in flux in the [Ca II]-dominated F814W filter (10%) compared to the other broadband filters (20%–30%) is significant (see Figures 9 and 8, upper middle panel). A likely explanation for this is that a significant fraction of the [Ca II] emission comes from excitation through the resonant H & K lines at 3934 and 3968  $\text{\AA}$  by fluorescence, which one decreases over time (Li & McCray 1993; Kozma & Fransson 1998). In contrast to the earlier epochs, where the flux in the H & K lines was dominated by the ejecta, the flux is now dominated by radiative shocks in the ER (see Fransson et al. 2013, and references therein). Scattering by the H & K lines gives rise to the triplet of Ca II lines at 8498, 8542, and 8662  $\text{\AA}$ , which in turn gives rise to the [Ca II]  $\lambda\lambda$  7293, 7326 emission lines. Therefore, the emissions in the doublet and triplet should be of the same order. The triplet is not observed in the STIS spectra (see Figure 3) because of the low S/N of the spectra in this wavelength range. However, it is observed in newly acquired MUSE spectra that will be discussed in a forthcoming paper (C. Fransson et al. 2024, in preparation), which supports this interpretation. The fact that the contribution from this process has decreased with time—as the ER has faded by a factor of  $\sim 2$  between the two considered epochs—explains that the flux in the F814W filter has increased less than the flux in the hydrogen-dominated filters.

For the Mg II emission that dominates the F275W and F280N filters, the ejecta morphology is rather different than the morphology in the other filters. Notably, the Mg II emission is brighter in the western and eastern regions between the inner ejecta and ER, fainter in the southern ejecta close to the ER, and fainter in the central region just south of the hole (see Figures 4 and 5). A major reason for this is that the Mg II  $\lambda\lambda$  2795, 2802 lines are optically thick, so their emission indicates where they are last scattered rather than emitted. Kangas et al. (2022) found that these lines are primarily powered by X-rays from the ER (which can explain the bright emission in the western ejecta, as discussed for all the filters in Section 7.1) but

with a significant ( $\sim 1/3$ ) contribution from the pumping of the Mg II 1239, 1240 Å transition by redshifted Ly $\alpha$  (1216 Å).

Given the difference in wavelength with the Mg II  $\lambda$  1240 line, the Ly $\alpha$  line responsible for the pumping cannot be emitted from the same location as the Mg II line, but has to come from a region receding from the Mg II location with a relative velocity between 5981 and 6097 km s<sup>-1</sup>, corresponding to a redshift of 24.26–24.73 Å. Because of the damping of the wings of the Ly $\alpha$  line (see Figure 4; and related discussion in Kangas et al. 2022), these values are upper limits only as a nonnegligible part could come from longer wavelength Ly $\alpha$  photons, that is to say, lower redshift photons.

Given the expansion of the ejecta, the Ly $\alpha$  photons important for the Mg II emission are emitted by close to diametrically opposed regions.<sup>14</sup> The absence of Mg II emission in the central part of the ejecta most probably implies that there is no such Ly $\alpha$  emission region having the correct redshift to produce the Mg II emission. Another explanation (not exclusive) could be that the region is optically thick to the Ly $\alpha$  photons, which prevents the Mg II emission in this central region. This was indeed found by Jerkstrand et al. (2011) at 2875 days after the explosion, but since then, the optical depth has gone down over time because of the expansion.

The obvious candidate for the origin of the Mg II line emission in the inner ejecta is the Ly $\alpha$  emission in the reverse shock, as the latter is known to emit strong Ly $\alpha$  and to extend to velocities of  $\sim 10,000$  km s<sup>-1</sup> (France et al. 2011). Further, the reverse shock emission is mainly blueshifted in the north and redshifted in the south (see, e.g., France et al. 2015; Kangas et al. 2022; Larsson et al. 2023).

Figure 5 of Larsson et al. (2023) shows that the regions having the highest radial velocities 12,927 days after the explosion are located in the southeast reverse shock, which is consistent with the highest Mg II emission arising in the western part of the ejecta. This is also illustrated in Figures 15 and 16 of Larsson et al. (2019a) showing contours in velocities in the reverse shock in agreement with the previous assertion.

According to Michael et al. (2003), the Ly $\alpha$  photons from the reverse shock will not easily traverse the ER back and propagate to the center. However, the photons that undergo scattering toward the center will be redshifted by the correct amount (up to a velocity of 12,000 km s<sup>-1</sup>, Michael et al. 2003; Larsson et al. 2019a) and contribute to the Mg II emission, consistent with Kangas et al. (2022).

In addition, the NV  $\lambda\lambda$  1239, 1243 lines emitted by the reverse shocks might also contribute to the Mg II fluorescence, although to a lower extent than the Ly $\alpha$  emission, as discussed in Kangas et al. (2022). Given the wavelengths of the NV lines, these lines should be emitted in a region of the reverse shocks that have no (or very small) velocity shift compared to the considered part of the ejecta. We therefore conclude that the conditions are met for the Ly $\alpha$  and NV lines to contribute to the observed Mg II emission.

### 7.3. Asymmetric Distribution of the Ejecta

The asymmetric distribution of the ejecta observed at late times carries the imprints of the explosion mechanism and progenitor structure, as shown by numerical simulations (Ono et al. 2020; Orlando et al. 2020; Gabler et al. 2021). The best observational constraints on the ejecta morphology in SN 1987A have been obtained from integral field unit data and long-slit spectroscopy, which provide 3D information for individual emission lines (Kjær et al. 2010; Larsson et al. 2016, 2019b; Kangas et al. 2022; Larsson et al. 2023). In contrast, the morphology observed in images is more difficult to interpret due to projection effects, blending of different emission lines in broadband filters, as well as incomplete coverage of the broad ejecta lines in the narrowband filters. The HST images analyzed here do, however, provide an important complement to the 3D results by providing detailed information about the time evolution, better spatial resolution, as well as a wider wavelength coverage.

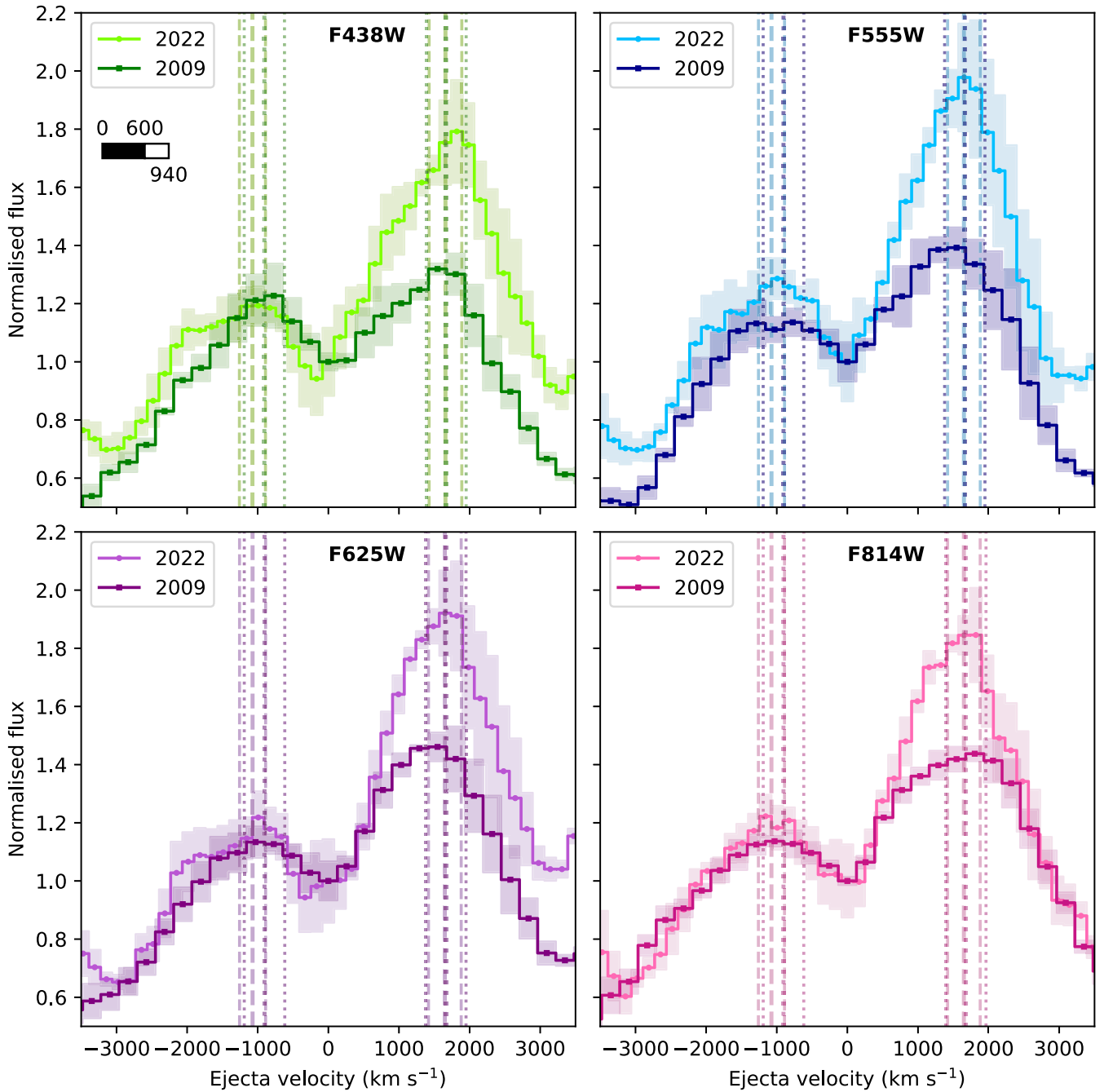
Figure 10 and Appendix Figure 16 illustrate the time evolution of the ejecta and include the expanding aperture used for measuring the ejecta flux. The outer edges of the bright inner ejecta remain at the same relative position with respect to this aperture, as expected for homologous expansion (e.g., the bright extension to the west that just reaches the edge of the aperture at all epochs).

To quantify the homologous expansion, we adopted a horizontal region centered on the geometric center of SN 1987A covering the inner ejecta from east to west and with a width in the north–south direction of 0".15 in the 2022 observations (see Figure 2). For each position in the east–west direction, we computed the median flux and associated standard deviation over the pixels in the north–south direction. We adopted the same procedure for the 2009 observations except that the width in the north–south direction was scaled by the ratio between days since the explosion to account for the homologous expansion. The results are shown for four different filters in Figure 13, where the position in the east–west direction has been converted into the expansion velocity following Equation (1). In these plots, the fluxes are in arbitrary units and were scaled by the corresponding flux in the central pixel for clarity. As Figure 13 shows, the two peaks, corresponding to the two brighter regions east and west of the center, are located at positions corresponding to expansion velocities of  $-1075 \pm 185$  and  $+1650 \pm 230$  km s<sup>-1</sup> in 2022, and  $-905 \pm 285$  and  $+1670 \pm 285$  km s<sup>-1</sup> in 2009, corresponding to the mean and standard deviation in all four filters presented in Figure 13. The fact that the peaks occur at very similar velocities at both epochs, consistent within  $1\sigma$ , strongly supports that the ejecta is in homologous expansion. The results for the other filters as well as for a region oriented in the north–south direction are very similar.

The main time evolution observed is the relative brightening of the western side compared to the eastern side, attributed to the energy input from X-rays from the ER (see Section 7.1). We note that the expansion implies that the spatial resolution (FWHM  $\sim 0".09$ ), expressed in terms of ejecta velocity following Equation (1), has improved from  $\sim 940$  to  $\sim 600$  km s<sup>-1</sup> over the epochs covered by Figure 10. While we observe spatial variations in the surface brightness down to the resolution level of WFC3 at all epochs (also illustrated in Figure 13), no new clearly separated substructures have emerged over the course of the observations. This indicates

<sup>14</sup> In comparing the Ly $\alpha$  emission with the Mg II emission, we should account for the temporal delay between the two emissions. For the ejecta region considered here, the maximum delay corresponds to the diameter of the ER divided by the speed of light, which is equal to 1.7 yr. However, the effect of this time delay is negligible for the comparisons that can be made based on the imaging data.





**Figure 13.** Normalized flux as a function of the position, converted into ejecta velocity with respect to the geometric center, in the east–west region, in 2022 and 2009 in the F438W, F555W, F625W, and F814W filters. The lines and shaded areas correspond to the median fluxes and corresponding standard deviations. The vertical dashed (resp. dotted) lines indicate the mean and standard deviation of the maxima of the corresponding 2022 (resp. 2009) curves. The scale bars in the top left panel indicate the velocity resolution corresponding to the FWHM of the spatial resolution at the two epochs.

that there are no well-defined clumps on this size scale or that any such clumps are hidden by projection effects in the images.

The comparison of the ejecta morphology at different wavelengths (see Figure 4) reveals the same overall elongation along an axis offset to the east from the north by  $\sim 15^\circ$ . This shows that the elements that dominate the thermal emission in different filters, that is to say, Mg (F275W), Fe (F336W and F438W), H (F555W and F625W), and Ca (F814W), are well mixed and follow the same large-scale geometry as has been seen in previous observations (Larsson et al. 2023, and references therein). The differences between filters that are

observed on a more detailed level are expected to reflect both smaller-scale spatial differences in ejecta abundances and the details of the emission line production. While the morphology of the Mg emission is clearly influenced by scattering effects (see Section 7.2), it is interesting to compare the filters dominated by Fe, H, and Ca. The corresponding images all show enhanced emission in the western ejecta. However, the H-dominated filters are relatively brighter in the region that extends farthest to the west near the midplane of the ER (see Figures 4 and 5), which is consistent with a radially increasing relative abundance of hydrogen.

#### 7.4. Constraints on the Compact Object

JWST observations of SN 1987A in the near-IR (NIR) and mid-IR showed strong evidence for a central source in emission lines of [S III-IV], [Ar II], and [Ar VI] (Fransson et al. 2024). The lines are narrow ( $\lesssim 300 \text{ km s}^{-1}$ ), and the source is spatially unresolved, showing that the emission region is small. The small, central emission region, the high ionization, and the fact that these lines were only seen in these intermediate elements indicate that this emission is coming from the explosive oxygen burning region, close to the newly formed neutron star. The exact nature of this emission is, however, not clear. The strongest candidates for the ionizing emission are either synchrotron emission from a PWN, formed as a result of the relativistic wind from the pulsar, or as a result of the ionizing radiation from the cooling, hot neutron star, or possibly from slow shocks as a result of the PWN bubble expanding into the ejecta. Photoionization models, reproducing the JWST lines, showed agreement with either the PWN model or the CNS model (Fransson et al. 2024).

While these models were only discussed in the context of the JWST observations, they also predict other lines in the UV, optical, and far-IR. In particular, they can be used to estimate the fluxes from lines in the observed HST filters. The strongest lines in these models are the [S II]  $\lambda\lambda$  4070, 4076, 6718, 6733, [S III]  $\lambda\lambda$  9071, 9533, [O III]  $\lambda\lambda$  4960, 5008, [Ar III]  $\lambda\lambda$  7138, 7753, and [Ar V]  $\lambda\lambda$  6437, 7007 lines. The main problem is the background from the general ejecta emission, as well as that of the outer rings and the reverse shock. Because of the expected line fluxes and especially the filter widths, the best prospect for detecting a compact object is the narrow F502N filter, containing the [O III]  $\lambda$  5008 line.

Using these models and tying them to the JWST observed fluxes, we can estimate the [O III]  $\lambda$  5008 flux. The total luminosity of the strong [Ar II] 6.998  $\mu\text{m}$  line is  $\sim 2.47 \times 10^{32} \text{ erg s}^{-1}$ , corresponding to a flux of  $\sim 8.39 \times 10^{-16} \text{ erg cm}^{-2} \text{ s}^{-1}$ . In the “standard” PWN model (Figure 4 in Fransson et al. 2024), the luminosity of the [O III]  $\lambda$  5008 line is  $4.8 \times 10^{-1}$  of the [Ar II] line, while that in the CNS model is much lower,  $1.7 \times 10^{-2}$  of the [Ar II] line. The fluxes therefore correspond to  $\sim 4.03 \times 10^{-16} \text{ erg cm}^{-2} \text{ s}^{-1}$  and  $\sim 1.43 \times 10^{-17} \text{ erg cm}^{-2} \text{ s}^{-1}$ , respectively, in the two models.

There is no point source detected in the F502N filter, so we placed an upper limit on the detection of a point source by adding artificial point sources using the DAOSTarFinder routine from the photutils.detection package in python. We assumed a Gaussian PSF with a FWHM determined from nearby stars. We used a Monte Carlo technique to generate point sources within  $3\sigma$  of the position of the [Ar VI] source, which has the most accurate position of the lines detected by JWST, being located  $38 \pm 22 \text{ mas}$  east and  $31 \pm 22 \text{ mas}$  south of the center of the ER (with  $1\sigma$  uncertainties, Fransson et al. 2024). Our results show that the highest  $3\sigma$  limit within this region is  $6.5 \times 10^{-18} \text{ erg cm}^{-2} \text{ s}^{-1}$ , which we take as the limit on a [O III] emitting point source associated with the JWST source. Considering all the limits in the region, we find that sources of  $3.6 \times 10^{-18}$  to  $6.5 \times 10^{-18} \text{ erg cm}^{-2} \text{ s}^{-1}$  have at least 90% probability of detection, and sources fainter than  $0.9 \times 10^{-18} \text{ erg cm}^{-2} \text{ s}^{-1}$  have a zero probability to be detected. The upper limits on a point source are lower than both PWN and CNS model predictions.

There are several caveats with this comparison. First, the model fluxes are sensitive to the ionizing spectrum, as is clearly

seen when comparing these two models. This is positive when using these lines as diagnostics of the ionizing spectrum and therefore the general scenario. However, there are uncertainties in the PWN spectrum, where the synchrotron power law of a very young PWN may differ from that of the Crab PWN assumed here, as well as in the temperature of the neutron star.

A major uncertainty is the abundances of elements in the zone with high S and Ar abundances, which can be seen in Figure S7 in Fransson et al. (2024). For the  $19 M_{\odot}$  zero-age main sequence model, this extends from 1.77 to  $2.10 M_{\odot}$ . However, while the S and Ar abundances are high over this whole zone, the O abundance is  $\lesssim 10^{-4}$  (in number) in the inner  $0.11 M_{\odot}$  of this zone, while it increases to  $\sim 0.6$  in the outer  $0.21 M_{\odot}$  of the zone. Because the JWST observations are mainly sensitive to the heavier elements, it is difficult to distinguish these zones solely from these observations. However, the different O abundances in the two regions produce widely different results for the [O III] line. The nondetection of this line can therefore be an indication that the emission seen with JWST originates from the inner of these S- and Ar-rich zones.

Alternatively, the dust in the ejecta might affect the observed flux. The distribution, composition, and optical depth of this dust are uncertain (see Fransson et al. 2024). For pure silicates, the absorption in the optical and NIR ranges is low, but scattering might be important, depending on the size of the grains (e.g., Tamanai et al. 2017). The effect of scattering is to both give a spatially more extended distribution and broaden the line in wavelength, if there are multiple scatterings. The total flux would, however, not be affected. However, if the silicates contain even low fractions of other elements, like carbon or iron, the absorption part of the refractive index increases, and the absorption might become important also for the optical range (Dorschner et al. 1995).

In the scenario where pure scattering spreads out the photons of the point source but does not affect the total flux, it is interesting to compare the model predictions with the total flux in the central region in the F502N filter. The measured flux density is  $0.46 \times 10^{-17} \text{ erg cm}^{-2} \text{ s}^{-1} \text{ \AA}^{-1}$  (see Table 4), which corresponds to a flux of  $\sim 3.0 \times 10^{-16} \text{ erg cm}^{-2} \text{ s}^{-1}$  for an effective width of  $65 \text{ \AA}$ . The predicted flux from the PWN model in the [O III] line is therefore 134% of the total, while it is only 4.76% for the CNS model. If we subtract the maximum possible contamination from the northern outer ring in this region (see Appendix C), the predicted fluxes correspond to 249% and 8.81%, respectively. This indicates that only the CNS model is consistent with the observations if the assumption of a point source is removed, with the caveat that we do not know the size of the region over which the flux will be distributed due to scattering.

The contribution from the lines associated with the compact object to the other filters is expected to be smaller than in F502N, so it is not surprising that the photometry of the central region does not reveal any evidence of an additional energy source, showing the same shape but a smaller flux increase with time compared to the surrounding ejecta (see Figure 9). Similarly, as the light curves in the F438W and F625W filters contain strong, broad lines from the ejecta, it is not surprising that they do not show any increase in the central region due to the compact object.

## 8. Conclusion

SN 1987A is the most thoroughly studied SN so far thanks to the spatially resolved view of the transition into a young SNR that it offers. In this paper, we have analyzed the HST images taken at day 12,980 after the explosion. These new images cover the whole wavelength range between  $\sim 2000$  and  $\sim 11000$  Å for the first time since day 8329 after the explosion. We studied both the broadband and narrowband photometry and morphology of the ER, the ejecta, and the central region at this new epoch and provided comparisons with the previous one. We also analyzed the light curves of the SN in the F438W and F625W filters and added four more epochs to the latest light curves provided in the literature.

The ER has followed its slow fading route over the whole wavelength range covered by our observations (see Figure 9) and shows a flux at day 12,980 about half of the flux at day 8329. The eastern part has faded more than the western part by about 10%–20%. We also find a reversal in the time evolution of the ratio between western and eastern parts fluxes in the ER: while this ratio increased until  $\sim 11,000$  days after the explosion, it started to decrease afterwards, although the western part is still a factor of 2 brighter than its eastern counterpart.

The ejecta showed a light curve that started to flatten around day 11,000 after the explosion. Overall, the ejecta have proportionally brightened less between epochs 8329 and 12,980 (by a factor of 1.1–1.3 in  $\sim 4650$  days) than between epochs 5400 and 7200 (where it brightened by a factor of 2.6 in  $\sim 1800$  days). This can be attributed to less energy input from X-rays from the ER at late times; the soft X-ray light curve declines after day  $\sim 10,000$ , and the hard X-ray light curve flattens since day  $\sim 12,000$  after the explosion. The western part of the ejecta is brighter than the eastern part, consistent with the western ER being brighter in the X-rays than the eastern part. The ejecta have brightened less in the F814W filter than in the other broadband filters because the emission in this filter comes principally from [Ca II], which is likely partly excited by the fading optical emission from the ER.

The emission in the ejecta follows homologous expansion. The morphology is clearly asymmetric, and the ejecta are well mixed on large scales, as evident from the very similar morphology observed in all filters, which probe emission lines from different elements, including H, Fe, and Ca. Only one broadband filter stands out from this picture: F275W. The difference in morphology observed in the F275W filter is attributed to the different mechanism producing the Mg II  $\lambda\lambda$  2795, 2802 lines, as well as the fact that these lines are optically thick. These lines are partly formed through pumping by the Ly $\alpha$  and, to a smaller extent, the N V  $\lambda\lambda$  1239, 1243 photons from the reverse shock, as well as by thermalization of X-rays coming from the ER.

Finally, we searched for emission associated with the compact object in view of recent JWST observations of SN 1987A in the NIR and mid-IR that show a central source. However, the HST observations do not show any sign of a compact object, neither in the morphology, nor in the

photometry, nor in the light curves. The models discussed in the context of the JWST observations predict a relatively strong [O III]  $\lambda$  5008 line. We used the F502N observation containing this line to put a  $3\sigma$  upper limit on a point source of  $6.1 \times 10^{-18}$  erg s $^{-1}$  cm $^{-2}$ . This value being lower than both CNS and PWN model predictions, it does not favor the CNS nor the PWN as the ionizing source. However, there are several caveats in the model predictions, and the current observations are fully consistent with the CNS model in the scenario that dust scattering spreads the emission over a larger region. The nondetection of the [O III]  $\lambda$  5008 line can also be an indication that the emission seen with JWST originates from the inner part of the S- and Ar-rich zones.

In the future, we hope to continue the monitoring in F502N and other filters to try to detect the presence of the compact object. The probability of detecting optical emission associated with the compact object increases with time as the optical depth of the dust decreases.

The reverse shocks will be addressed in a forthcoming paper: Their properties will be determined through the analysis of the time evolution and modeling of the UV spectrum. This will allow us to gain information about the shock physics and the properties of the CSM, the latter probing the mass-loss history of the progenitor including the formation of the rings.

## Acknowledgments

S.R. warmly thanks Prof. G. Rauw and Dr. D. Alp for constructive discussions. Support for HST GO program Nos. 11653, 12241, 13181, 13405, 13810, 14333, 14753, 15256, 15503, 15928, 16265, and 16789 was provided by NASA through grants from the Space Telescope Science Institute, which is operated by the Association of Universities for Research in Astronomy, Inc., under NASA contract NAS5-26555. M.M. acknowledges support from STFC Consolidated grant (ST/W000830/1).

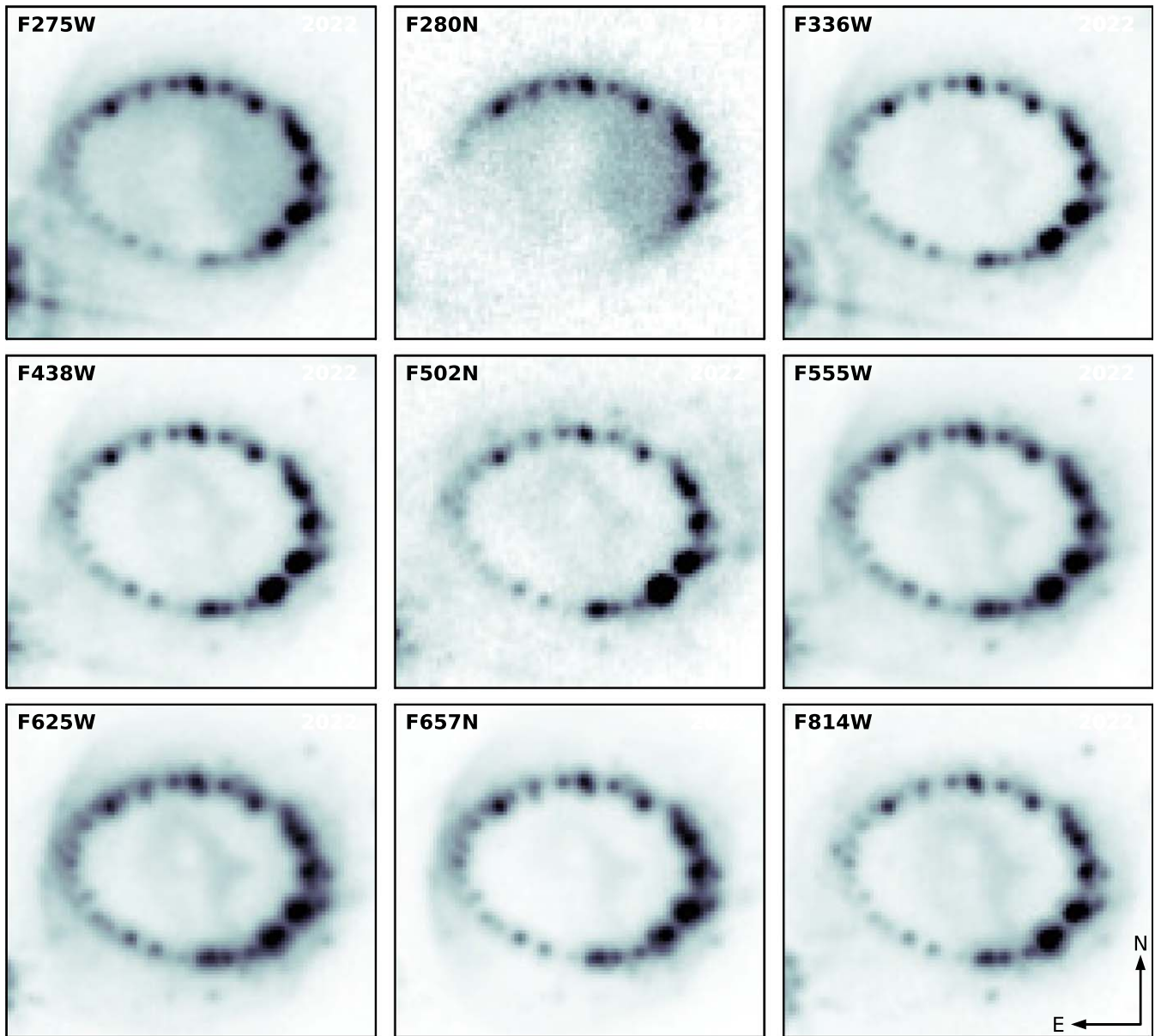
Data presented in this article were obtained from the Mikulski Archive for Space Telescopes (MAST) at the Space Telescope Science Institute. The specific observations analyzed can be accessed via doi:[10.17909/vv4m-mm08](https://doi.org/10.17909/vv4m-mm08).

*Facility:* HST (WFC3).

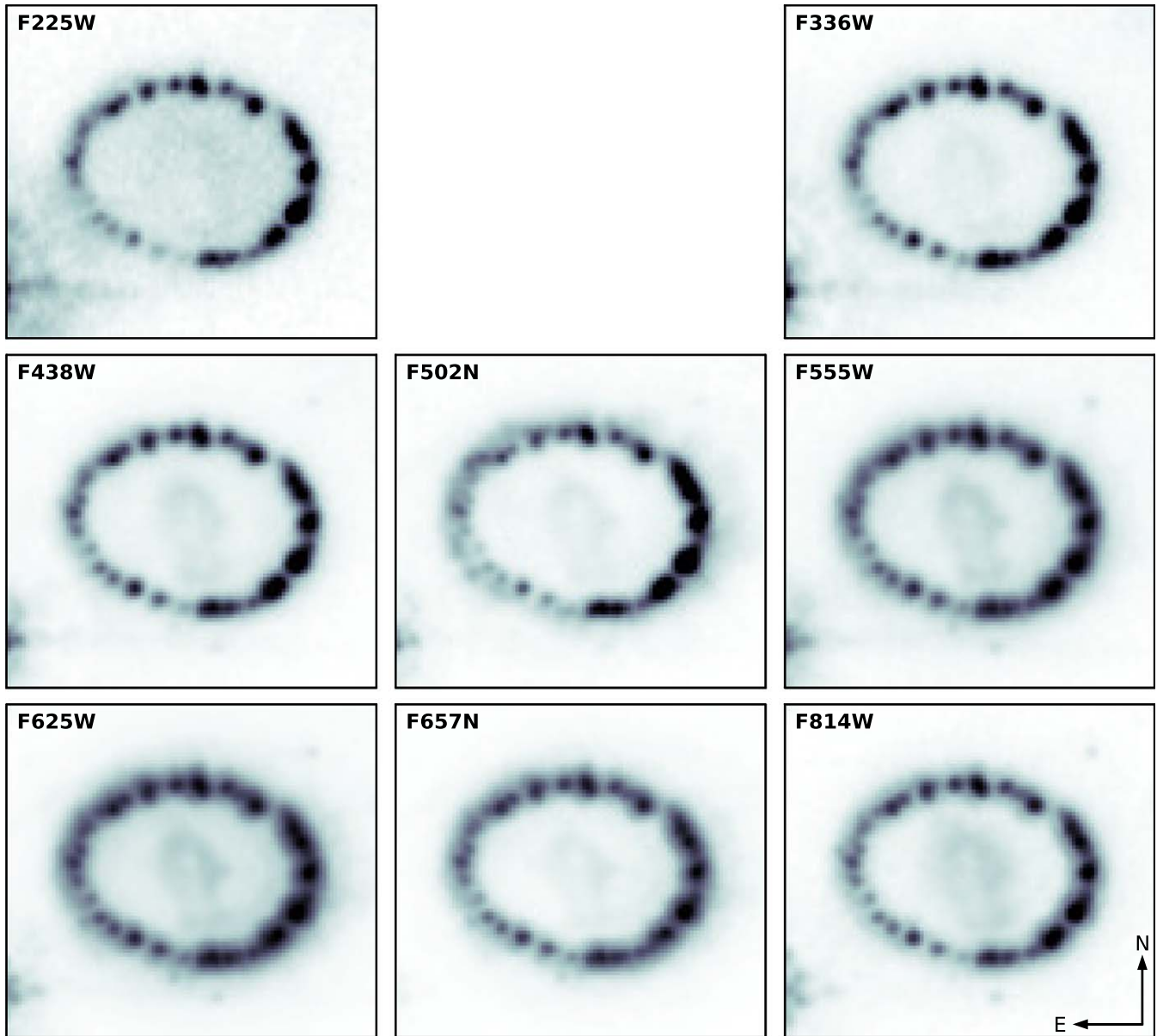
*Software:* astropy (Astropy Collaboration et al. 2013, 2018, 2022), DrizzlePac (Ferland et al. 2013), matplotlib (Bertin & Arnouts 1996), Photutils (Bradley 2023), scipy (Virtanen et al. 2020).

## Appendix A Additional Figures

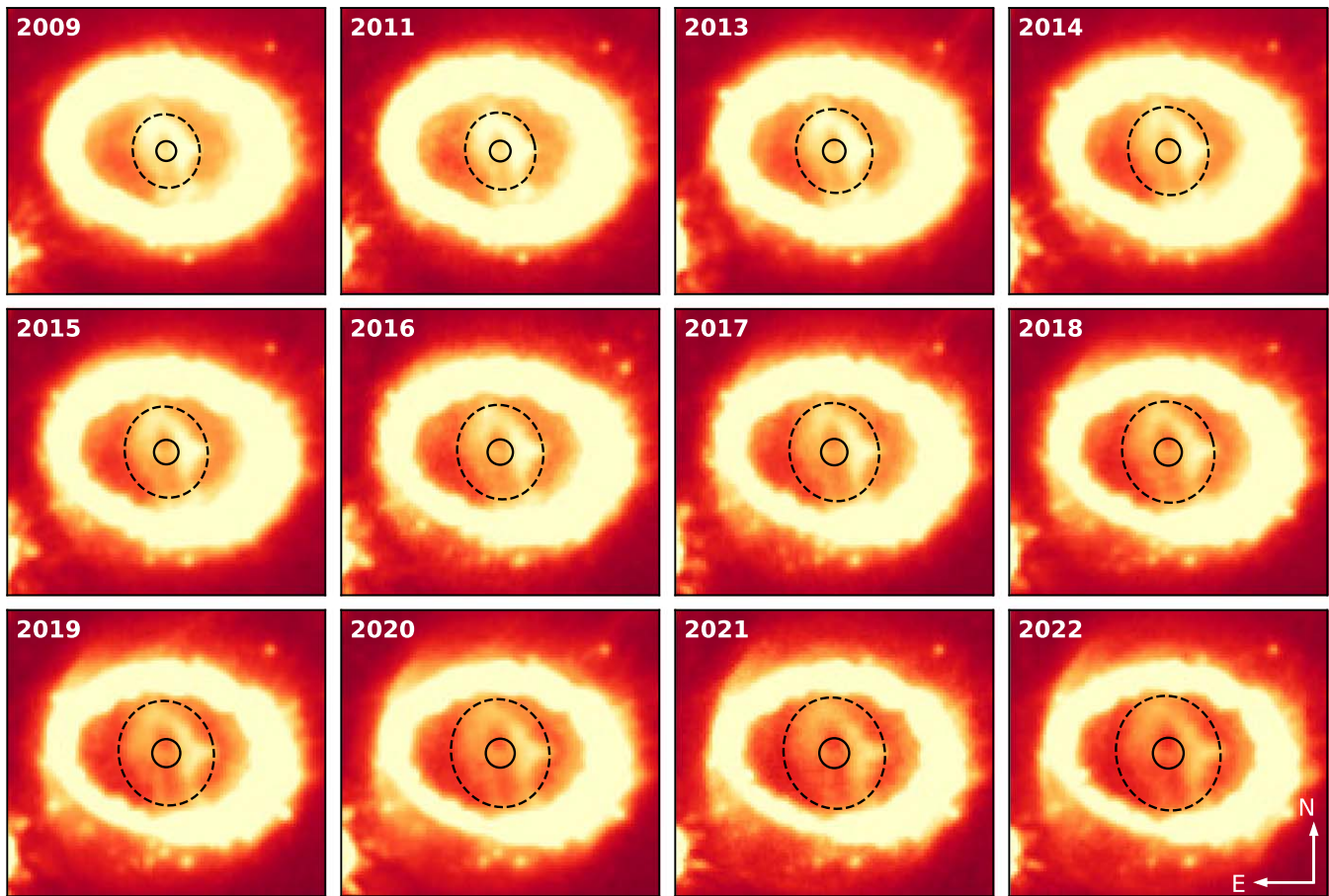
This section presents the HST observations at days 12,980 (Figure 14) and 8329 (Figure 15) in all filters with a color scale optimized to highlight the hotspots in the ER and between days 8329 and 12,980 in the F625W filter with a color scale optimized to highlight the emission in the ejecta (Figure 16) and in the F438W and F625W filters (Figure 17) with a color scale optimized to highlight the hotspots in the ER.



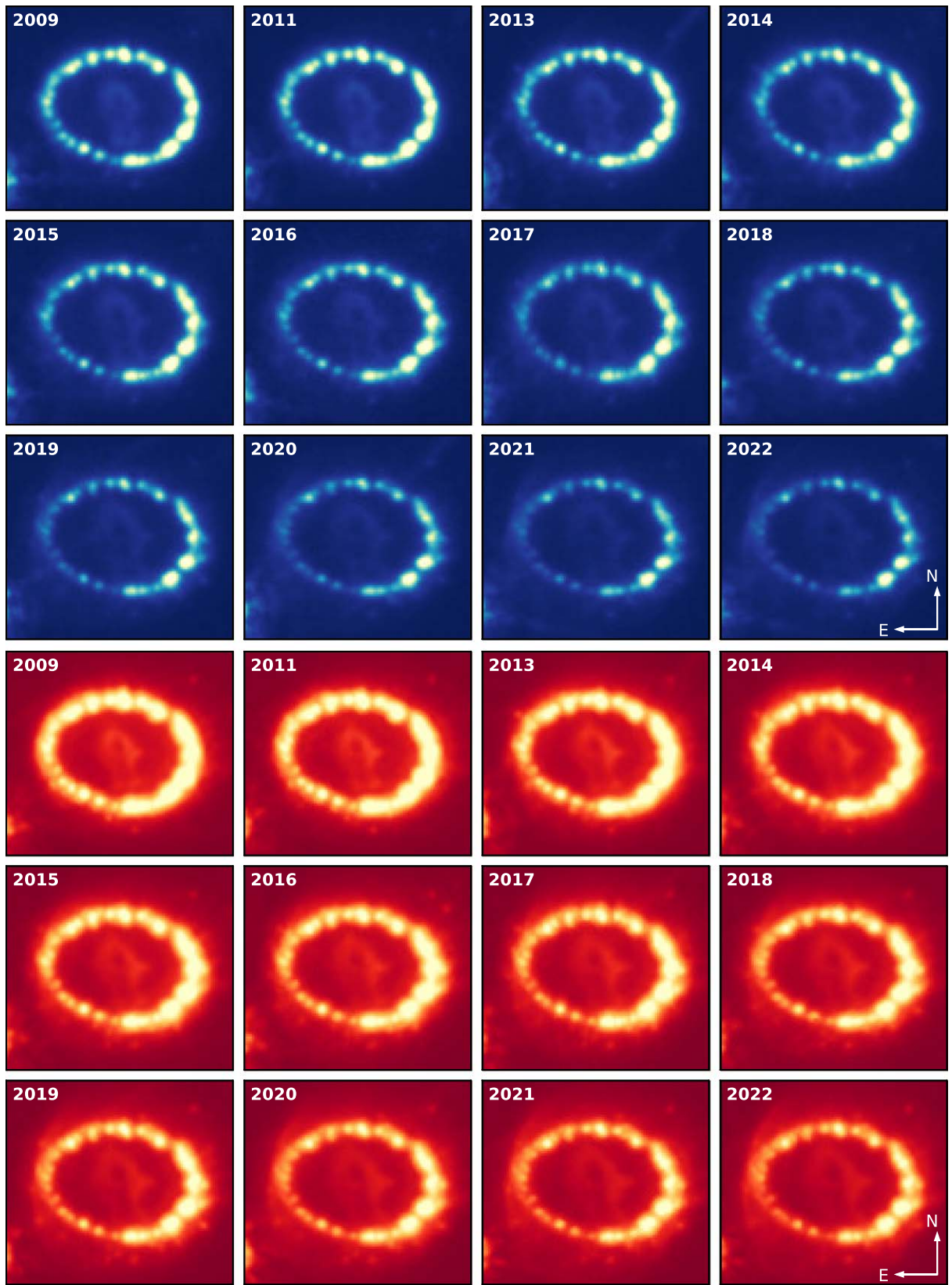
**Figure 14.** HST/WFC3 images of SN 1987A taken 12,980 days after the explosion in nine different filters. The images were scaled by an asinh function, and the color scales were chosen differently for each filter to highlight the hotspots in the ER. The field of view for each image is  $2''.50 \times 2''.25$ .



**Figure 15.** HST/WFC3 images of SN 1987A taken 8329 days after the explosion in eight different filters. The images were scaled by an asinh function, and the color scales were chosen differently for each filter to highlight the hotspots in the ER. The field of view for each image is  $2''.50 \times 2''.25$ .



**Figure 16.** HST/WFC3 images showing the evolution of SN 1987A in the F625W filter between epochs 8329 and 12,980 (labeled by the year of observation). The emission in the lower left corner is due to Star 3 (see Figure 1). The images were scaled by an asinh function to highlight the weak emission in the ejecta. The field of view for each image is  $2''.50 \times 2''.25$ . The black circle and dashed black ellipse overplotted on each image represent the center and ejecta regions, respectively, adopted to compute the fluxes. These regions grow in size from 2009 to 2022, using Equation (1) to define a comoving volume that tracks the same expanding ejecta with time.



**Figure 17.** HST/WFC3 images showing the evolution of SN 1987A in the F438W (top three rows) and F625W (bottom three rows) filters between epochs 8329 and 12,980 (labeled by the year of observation). The emission in the lower left corner is due to Star 3 (see Figure 1). The images were scaled by an asinh function. The field of view for each image is  $2''.50 \times 2''.25$ .

## Appendix B ER Contribution to the Ejecta and Center

In this appendix, we describe how the contribution of the ER to the ejecta and center was removed for all observations. The ER is indeed more than an order of magnitude brighter than the ejecta, which means that the scattered light from the ER—the extended wings of the PSFs of the hotspots—significantly contributes to the background in the ejecta.

We constructed a synthetic ER aiming at reproducing the ER for each epoch based on the locations of the 28 bright spots in the ER<sup>15</sup> (C. Tegkelidis et al. 2024, in preparation). We used the `Tiny Tim` HST PSF modeling tool to generate PSFs at the locations of the spots of which amplitudes are given by the relative brightnesses of the spots (C. Tegkelidis et al. 2024, in preparation). We adopted the corresponding filters and the 2017 spectra of the ER (Kangas et al. 2022) to generate the PSFs. The total flux of the synthetic ER was then scaled to match the observations. We here stress that, although the synthetic ER does not perfectly reproduce the observed ER, it does not significantly affect the correction for ER light contributing to the ejecta apertures as long as point sources with the correct total flux are placed in an ellipse, as discussed in Larsson et al. (2019a).

Based on these synthetic ERs, we computed the total contribution of the ER to the corresponding ejecta and center regions. We removed these contributions from the total ejecta and center count rates. We found that the fluxes were reduced by a nonnegligible amount, as summarized in Table 7 for the epochs 12,980 and 8329 observations and in

**Table 7**

Reduction of the Flux (in %) in the Ejecta and Center Regions after Removal of the ER Contribution in the Images at Epochs 12,980 and 8329 in the Different Filters

Filter	Epoch 12,980 Days		Epoch 8329 Days	
	Ejecta	Center	Ejecta	Center
F225W	...	...	10.0	9.1
F275W	9.7	8.8	...	...
F280N	7.4	7.8	...	...
F336W	16.5	14.8	16.7	15.7
F438W	12.6	11.8	10.6	11.0
F502N	10.7	10.5	12.3	13.9
F555W	12.5	9.4	10.6	9.3
F625W	14.1	9.6	12.5	9.6
F657N	20.8	14.0	19.1	14.3
F814W	9.1	6.7	7.0	6.3

<sup>15</sup> We note that we only consider the hotspots in the main ring, not new spots appearing farther out at later times.

**Table 8**

Reduction of the Flux (in %) in the Ejecta and Center Regions after Removal of the ER Contribution in the F438W and F625W Filters in the Images between Epochs 8717 and 12,598

Epoch (days)	Filter F438W		Filter F625W	
	Ejecta	Center	Ejecta	Center
8717	11.2	11.9	12.6	9.8
9480	11.7	11.8	12.9	9.6
9974	12.0	12.1	13.2	9.7
10,317	12.1	12.6	13.3	9.9
10,698	12.0	12.0	13.4	9.6
11,119	11.9	11.7	13.2	9.4
11,458	12.4	12.0	13.8	9.7
11,837	12.5	11.6	14.0	9.7
12,218	12.3	11.3	13.9	9.2
12,598	12.3	11.6	14.2	9.7

Table 8 for the observations from epoch 8717 to 12,598 included.

## Appendix C Outer Ring Contribution to the Ejecta and Center

In this appendix, we provide the estimated contribution of the northern outer ring to the ejecta and center regions at epochs 12,980 and 8329 in the different filters (see Table 9). These contributions were estimated using the brightest and faintest parts of the northern outer ring (northeast and southwest) as minimum and maximum fluxes, adopting the same number of pixels as in the ejecta and center regions. It is expected that the

**Table 9**

Estimated Contribution (in %) of the Northern Outer Ring to the Ejecta and Center Regions at Epochs 12,980 and 8329 in the Different Filters

Filter	Epoch 12,980 Days		Epoch 8329 Days	
	Ejecta	Center	Ejecta	Center
F225W	...	...	0–5	1
F275W	1–2	5–8	...	...
F280N	0–1	0–2	...	...
F336W	2–6	8–19	1–9	3–18
F438W	1–5	5–17	0–7	1–15
F502N	4–13	15–46	3–11	8–25
F555W	2–4	6–13	1–6	2–12
F625W	2–3	5–10	1–4	3–8
F657N	2–5	7–15	2–5	4–10
F657N	2–5	7–15	2–5	4–10
F814W	1	3–4	1	1–3

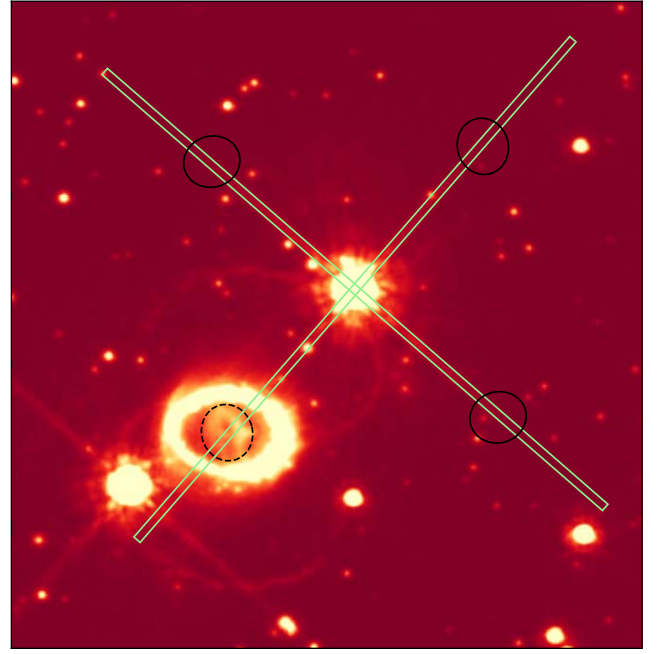


contribution from the northern outer ring lies in the ranges provided in Table 9, but we note that we did not correct the computed fluxes for it since we do not know the exact values of the contributions. Given that the dust in the central ejecta may scatter and absorb light from the outer ring, the actual outer ring contribution may be even lower than these limits.

### Appendix D Diffraction Spike Contributions

In this appendix, we describe how the diffraction spike contributions to the ejecta, center, and ER regions were removed. The center region is affected by a diffraction spike from Star 2 at epochs 11,119 and 12,218 (see Figures 10 and 16). The ejecta region is affected by a diffraction spike from Star 2 at epochs 9480, 11,119, and 12,218, and from Star 3 at epochs 8717, 11,458, and 11,837 (see Figures 10 and 16). The ER region is affected by a diffraction spike from Star 2 at epochs 9480, 11,119, 11,837, and 12,218, and from Star 3 at epochs 8717, 9480, 9974, 10,317, 11,119, 11,458, 11,837, and 12,218 (see Figures 10 and 16).

To account for these artifacts, we computed the fluxes in the three intersection regions between the three diffraction spikes that do not cross the center, ejecta, or ER region, and the corresponding center, ejecta, or ER region rotated by  $90^\circ$ ,  $180^\circ$ , and  $270^\circ$  with respect to the center of the considered Star 2 or 3 (see an illustration for the observation at day 12,218 in the F625W filter in Figure 18). We adopted a 5 pixel width for the diffraction spikes. For each observation and each considered region, we then averaged the computed fluxes to get an estimate of the diffraction spike contribution to the region. We discarded the diffraction spikes that were contaminated by either a star in



**Figure 18.** HST/WFC3 image of SN 1987A at day 12,218 in the F625W filter illustrating how the diffraction spike contribution (from Star 2 in this case) was estimated. The green rectangles represent the diffraction spikes regions, the dashed black ellipse represents the ejecta region, and the plain black ellipses represent the ejecta region rotated by  $90^\circ$ ,  $180^\circ$ , and  $270^\circ$ . The image was scaled by an asinh function. The field of view is  $9''.50 \times 9''.75$ .


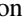
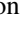
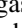
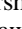
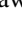
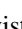

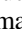


the field or the outer ring of SN 1987A. The reduction of the fluxes after subtraction of the diffraction spike contributions to the ejecta, center, and ER regions is given in Table 10.

**Table 10**

Reduction of the Flux (in %) in the Ejecta, Center, and ER Regions after Removal of the Diffraction Spike Contributions from Stars 2 and 3 in the F438W and F625W Filters in the Images between Epochs 8717 and 12,218

Epoch (days)	Ejecta			Center			ER		
	F438W	F625W	Star	F438W	F625W	Star	F438W	F625W	Star
8717	2.25	0.83	3	...	...	...	0.29	0.09	3
9480	0.59	0.56	2	...	...	...	0.80	0.24	2 and 3
9974	...	...	...	...	...	...	0.17	0.05	3
10,317	...	...	...	...	...	...	0.16	0.05	3
11,119	1.18	1.06	2	2.72	2.24	2	0.67	0.23	2 and 3
11,458	3.13	1.10	3	...	...	...	0.36	0.11	3
11,837	3.91	1.25	3	...	...	...	0.54	0.23	2 and 3
12,218	1.34	1.22	2	4.58	3.92	2	1.42	0.46	2 and 3

## ORCID iDs

Sophie Rosu  <https://orcid.org/0000-0002-2461-6913>  
 Josefin Larsson  <https://orcid.org/0000-0003-0065-2933>  
 Claes Fransson  <https://orcid.org/0000-0001-8532-3594>  
 Tuomas Kangas  <https://orcid.org/0000-0002-5477-0217>  
 Robert P. Kirshner  <https://orcid.org/0000-0002-1966-3942>  
 Stephen S. Lawrence  <https://orcid.org/0000-0002-7491-7052>  
 Peter Lundqvist  <https://orcid.org/0000-0002-3664-8082>  
 Mikako Matsuura  <https://orcid.org/0000-0002-5529-5593>  
 Jesper Sollerman  <https://orcid.org/0000-0003-1546-6615>  
 George Sonneborn  <https://orcid.org/0000-0003-1440-9897>  
 Linda Tenhu  <https://orcid.org/0000-0002-7746-8512>

## References

- Alp, D., Larsson, J., & Fransson, C. 2021, *ApJ*, 916, 76  
 Alp, D., Larsson, J., Fransson, C., et al. 2018, *ApJ*, 864, 174  
 Arendt, R. G., Boyer, M. L., Dwek, E., et al. 2023, *ApJ*, 959, 95  
 Arnett, W. D., Bahcall, J. N., Kirshner, R. P., & Woosley, S. E. 1989, *ARA&A*, 27, 629  
 Astropy Collaboration, Price-Whelan, A. M., Pey Lian, L., et al. 2022, *ApJ*, 935, 167  
 Astropy Collaboration, Price-Whelan, A. M., Sipőcz, B. M., et al. 2018, *AJ*, 156, 123  
 Astropy Collaboration, Robitaille, T. P., Tollerud, E. J., et al. 2013, *A&A*, 558, A33  
 Bertin, E., & Arnouts, S. 1996, *A&AS*, 117, 393  
 Bradley, L., 2023 *astropy/photutils*: 1.8.0, v1.8.0, Zenodo, doi:10.5281/zenodo.7946442  
 Cardelli, J. A., Clayton, G. C., & Mathis, J. S. 1989, *ApJ*, 345, 245  
 Cendes, Y., Gaensler, B. M., Ng, C.-Y., et al. 2018, *ApJ*, 867, 65  
 Cigan, P., Matsuura, M., Gomez, H. L., et al. 2019, *ApJ*, 886, 51  
 Crotts, A. P. S., & Heathcote, S. R. 2000, *ApJ*, 528, 426  
 Dorschner, J., Begemann, B., Henning, T., Jaeger, C., & Mutschke, H. 1995, *A&A*, 300, 503  
 Ferland, G. J., Porter, R. L., van Hoof, P. A. M., et al. 2013, *RMxAA*, 49, 137  
 France, K., McCray, R., Fransson, C., et al. 2015, *ApJL*, 801, L16  
 France, K., McCray, R., Penton, S. V., et al. 2011, *ApJ*, 743, 186  
 Frank, K. A., Zhekov, S. A., Park, S., et al. 2016, *ApJ*, 829, 40  
 Fransson, C., Barlow, M. J., Kavanagh, P. J., et al. 2024, *Sci*, 383, 898  
 Fransson, C., Larsson, J., Migotto, K., et al. 2015, *ApJL*, 806, L19  
 Fransson, C., Larsson, J., Spyromilio, J., et al. 2013, *ApJ*, 768, 88  
 Gabler, M., Wongwathanarat, A., & Janka, H.-T. 2021, *MNRAS*, 502, 3264  
 Gonzaga, S., Hack, W., Fruchter, A., et al. 2012, *The DrizzlePac Handbook* (Baltimore, MD: STScI)  
 Gröningsson, P., Fransson, C., Lundqvist, P., et al. 2008, *A&A*, 479, 761  
 Jerkstrand, A., Fransson, C., & Kozma, C. 2011, *A&A*, 530, A45  
 Kangas, T., Fransson, C., Larsson, J., et al. 2022, *MNRAS*, 511, 2977  
 Kjær, K., Leibundgut, B., Fransson, C., Jerkstrand, A., & Spyromilio, J. 2010, *A&A*, 517, A51  
 Kozma, C., & Fransson, C. 1998, *ApJ*, 497, 431  
 Larsson, J., Fransson, C., Alp, D., et al. 2019a, *ApJ*, 886, 147  
 Larsson, J., Fransson, C., Kjær, K., et al. 2013, *ApJ*, 768, 89  
 Larsson, J., Fransson, C., Östlin, G., et al. 2011, *Natur*, 474, 484  
 Larsson, J., Fransson, C., Sargent, B., et al. 2023, *ApJL*, 949, L27  
 Larsson, J., Fransson, C., Spyromilio, J., et al. 2016, *ApJ*, 833, 147  
 Larsson, J., Spyromilio, J., Fransson, C., et al. 2019b, *ApJ*, 873, 15  
 Lawrence, S. S., Sugerman, B. E., Bouchet, P., et al. 2000, *ApJL*, 537, L123  
 Li, H., & McCray, R. 1993, *ApJ*, 405, 730  
 Maitra, C., Haberl, F., Sasaki, M., et al. 2022, *A&A*, 661, A30  
 Matsuura, M., Dwek, E., Barlow, M. J., et al. 2015, *ApJ*, 800, 50  
 Matsuura, M., Wesson, R., Arendt, R. G., et al. 2022, *MNRAS*, 517, 4327  
 McCray, R. 1993, *ARA&A*, 31, 175  
 McCray, R., & Fransson, C. 2016, *ARA&A*, 54, 19  
 Michael, E., McCray, R., Chevalier, R., et al. 2003, *ApJ*, 593, 809  
 Morris, T., & Podsiadlowski, P. 2007, *Sci*, 315, 1103  
 Morris, T., & Podsiadlowski, P. 2009, *MNRAS*, 399, 515  
 Ono, M., Nagataki, S., Ferrand, G., et al. 2020, *ApJ*, 888, 111  
 Orlando, S., Ono, M., Nagataki, S., et al. 2020, *A&A*, 636, A22  
 Panagia, N., Gilmozzi, R., Macchetto, F., Adorf, H.-M., & Kirshner, R. P. 1991, *ApJL*, 380, L23  
 Pietrzyński, G., Graczyk, D., Giallenne, A., et al. 2019, *Natur*, 567, 200  
 Plait, P. C., Lundqvist, P., Chevalier, R. A., & Kirshner, R. P. 1995, *ApJ*, 439, 730  
 Sonneborn, G., Pun, C. S. J., Kimble, R. A., et al. 1998, *ApJL*, 492, L139  
 Sugerman, B. E. K., Crotts, A. P. S., Kunkel, W. E., Heathcote, S. R., & Lawrence, S. S. 2005, *ApJS*, 159, 60  
 Tamanai, A., Pucci, A., Dohmen, R., & Gail, H.-P. 2017, *ApJ*, 845, 6  
 Tziamtzis, A., Lundqvist, P., Gröningsson, P., & Nasoudi-Shoar, S. 2011, *A&A*, 527, A35  
 Virtanen, P., Gommers, R., Oliphant, T. E., et al. 2020, *NatMe*, 17, 261